JOINT EUROPEAN TORUS JET

JET–P(91)45

M. Brusati, D. Bartlett, G. Bosia, J. Dobbing, A. Ekedahl, P. Froissard, C. Gormezano, C. Gowers, J. Jacquinot, N. Jarvis, A. Kaye, M. Lennholm, O. Naito, M. Pain, F. Paoletti, D. Pasini, M.C. Ramos de Andrade, G. Rey, F. Rimini, G. Sadler, P. Schild, T. Wade and JET Team

Lower Hybrid Current Drive Experiments on JET

Lower Hybrid Current Drive Experiments on JET

M. Brusati, D. Bartlett, G. Bosia, J. Dobbing, A. Ekedahl, P. Froissard, C. Gormezano, C. Gowers, J. Jacquinot, N. Jarvis, A. Kaye, M. Lennholm, O. Naito[1], M. Pain, F. Paoletti, D. Pasini, M.C. Ramos de Andrade, G. Rey[2], F. Rimini, G. Sadler, P. Schild, T. Wade and JET Team*

JET-Joint Undertaking, Culham Science Centre, OX14 3DB, Abingdon, UK

[1]JAERI, Naka Fusion Research Establishment Naka, Ibaraki 311-01, Japan
[2]CEN Cadarache, 13108 St Paullez Durance, France
** See Appendix 1*

Preprint of Paper to be submitted for publication in
Nuclear Fusion

LOWER HYBRID CURRENT DRIVE EXPERIMENTS ON JET

M. Brusati, D. Bartlett, G. Bosia, J. Dobbing, A. Ekedahl, P. Froissard, C. Gormezano, C. Gowers, J. Jacquinot, N. Jarvis, A. Kaye, M. Lennholm, O. Naito[a], M. Pain, F. Paoletti, D. Pasini, M. C. Ramos de Andrade, G. Rey[b], F. Rimini, G. Sadler, P. Schild, T. Wade.

JET Joint Undertaking, Abingdon, Oxon OX14 3EA, UK

[a]Jaeri, Naka Fusion Research Establishment,
Naka, Ibaraki 311-01, Japan

[b]CEN Cadarache, 13108 St Paul lez Durance, France

Abstract

The new JET Lower Hybrid Current Drive (LHCD) system has been operational during the 1990 experimental campaign; up to 1.6 MW at 3.7 GHz have been coupled to 2 and 3 MA plasmas in the limiter and X-point configurations. 20 sec long LH pulses have led to steady state plasma conditions with a 50 % drop in the loop voltage measured up to $\bar{n}_e = 2\ 10^{19}\ m^{-3}$. The broadening of the current profile is observed to increase with increasing electron density. Combined operation of Ion Cyclotron Resonance Heating (ICRH) and

LHCD has resulted in current drive efficiencies $\gamma = \bar{n}_e I_{CD} R / P_{LH}$ ~ 0.4 10^{20} m^{-2} A/W at volume averaged electron temperatures of 1.9 keV and stabilization of sawteeth up to 2.9 sec.

LHCD operation is associated with central electron heating at ~ 1 keV/MW at $\bar{n}_e$ ~ 1.8 10^{19} m^{-3}, while generating a hollow shell of suprathermal electrons, as measured by a newly installed Fast Electron Bremsstrahlung diagnostic.

Introduction

Lower Hybrid systems are foreseen for non inductive current drive and current profile control in fusion experiments of the next generation.

The potential of Lower Hybrid waves for non inductive current drive and current profile control has been clearly demonstrated in a variety of experiments. On PLT /1/ 520 kA of plasma current have been driven with 520 kW of LH power at $\bar{n}_e \simeq 10^{19}$ m^{-3}, using a narrow wave spectrum at 2.45 GHz. On Asdex /2/, suppression of sawteeth and the m = 1 instability was observed, followed by an increase in the central value of the electron temperature up to $T_{e0} \simeq 8$ keV. More recently, full current drive up to 1.5 MA has been achieved in JT-60 with 4.5 MW of LH power at 1.74 to 2.23 GHz using a multijunction type launcher /3/, and a favourable scaling of current drive efficiency with the electron temperature has been observed.

A degree of control of the current density profile in JET, leading eventually to sawtooth stabilization, can be achieved by launching a high directivity narrow spectrum of Lower Hybrid waves at 3.7 GHz. An LHCD system capable of launching 12 MW of LH power is being developed where the parallel phase spectrum can be adjusted from $n_{\parallel} = 1.4$ to $n_{\parallel} = 2.4$. In this paper the first results obtained on JET with a prototype LHCD system capable of generating LH power in excess of 4 MW are reported.

JET operation up to now has been very successful in producing high values of the triple fusion product $n_D \tau_E T_i \simeq 9\ 10^{20}\ m^{-3} keVs$, with equivalent Q_{DT} up to 0.7, for 10 MJ stored energy and a plasma volume in excess of 120 m^3 /4/. JET is therefore in a privileged position for undertaking a comprehensive study of current drive schemes in reactor relevant scenarios.

The layout of this paper is as follows. In section 1 the JET Lower Hybrid prototype system is briefly described. The experimental conditions and the diagnostic support for the 1990 LH campaign are summarized in section 2 and the experimental results are reported in section 3. Conclusions and details on further developments are then summarized in section 4.

1 - The JET Lower Hybrid prototype system

Results so far have been obtained with a LHCD prototype launcher consisting of 16 multijunctions resulting in 128 narrow

waveguides facing the plasma /5/. The launcher is powered by 8 klystrons capable of delivering up to 4 MW for 20 sec or 5.2 MW for 10 sec, via a low loss waveguide transmission line pressurized at 1 bar overpressure SF_6. The vacuum transition is made by means of a circular double quarter wavelength Be window (fig. 1).

The upper half of the multijunction is made in C coated CuZr with a short circuit in the fourth multijunction port, following a design developed in Cadarache for Tore Supra. The lower half consists of 8 C coated Cu coated Stailess Steel multijunctions packed together without gaps at the grill mouth, following a JET design. Each horizontal row of multijunctions consists of 16 waveguides. Built-in phase shifters give a $\pi/2$ phasing between adjacent waveguides of a given multijunction. The resulting wave spectrum is centred at $n_{\parallel} \simeq 1.8$ with a 70 % directivity (fig. 2); the peak $n_{\parallel}$ value can be varied from 1.4 to 2.4 by varying the phase between klystrons from $-\pi/2$ to $+\pi/2$, at the expense of the wave directivity.

The next LHCD system will consist of 24 klystrons feeding 48 multijunctions of the JET type. This system will be able to launch up to 10 MW of LH power and will be installed for operation in the Divertor phase of JET.

The launcher is assembled onto a main radial equatorial port of the JET vacuum vessel. It sits on movable legs and is capable of radial displacements during a plasma discharge of up to 210 mm via a bellow assembly, in order to maintain the density at the

grill mouth in the required range for proper matching (fig. 3).

Directional couplers allowing phase measurements are located in the pressurized part of the transmission line. Proper assessment of the phasing at the grill mouth has been achieved by varying the phase between 2 multijunction on a given row. The total reflected power in a multijunction is the sum of the contribution of the self reflection at the plasma, i.e. the S_{11} component of the scattering matrix and the power coupled via the plasma from the neighbouring multijunctions, corresponding to the S_{12} and S_{21} scattering matrix elements. The total reflected power is minimum when the two contributions have a π phase difference and for different phasing between multijunctions. Assuming $S_{12} = S_{21}$, it can be shown that the phase difference at the grill mouth between two multijunctions is given by the half sum of the phases corresponding to a minimum. In fig. 4 the evolution of the reflection coefficient on two multijunctions (a,b) is shown when the phase between the feeding klystrons is varied by a full cycle (e) during a pulse. Results of the theoretical simulation (c,d) are also shown for comparison.

During most of the experimental campaign the LH power waveform consisted of a 5 to 15 sec long flat-top preceeded by a 5 sec 100 % modulation phase at 2 Hz (fig. 18a), with a turn-on time ~ 1 ms, shorter than the data acquisition sampling time. This procedure allowed more efficient conditioning of multijunction and vacuum waveguides and has led to preliminary assessment of fast electrons dynamics.

2 - Experimental conditions and diagnostics

Lower Hybrid experiments on JET were performed on deuterium plasmas in limiter and double null X-point configuration at 2 and 3 MA of plasma current and 2.8 T toroidal field. The LH launcher position was varied with respect to the toroidal belt limiter and the neighbouring ICRH antenna to obtain high enough plasma density at the launcher mouth in order to provide good matching to the plasma while minimizing the power load from the plasma onto the C protection tiles. The launcher was positioned at the same major radius of the ICRH antenna in limiter discharges and from 10 to 20 mm behind in double null (DN) L-mode plasmas, which are characterized by wider scrape off layer and high edge density. The plasma-launcher interaction is monitored via a CCD camera equipped with a 8254 Å (Be I) filter, corresponding to the maximum infrared CCD sensitivity, viewing the launcher from the main upper vertical port (fig. 5). This system allows real time visual monitoring of RF breakdowns in the multijunction and of the plasma thermal load on the launcher mouth. Minimization of the thermal load, together with coupling considerations defines the optimum launcher radial position.

Preprogramming of the shaping field and position control feedback was required to match the plasma boundary to the launcher poloidal shape. When operating in conjunction with ICRH, fine position control could be achieved by feeding back the plasma radial position control on the ICRH coupling resistance at values

ranging between 4 and 6 ohms.

The behaviour of the plasma current density profile was monitored through the time evolution of the internal inductance and of the second Shafranov moment as derived from sets of magnetic pick-up coils and flux loops, installed at different poloidal sections of the torus, with the magnetic equilibrium reconstruction code IDENTC /6/.

The line average electron density, as measured by the multichannel FIR interferometer /7/ and by the LIDAR scattering system /8/, was varied between the values of 10^{19} m^{-3} and 2.5 10^{19} m^{-3}, and kept constant during the LH pulse. The level of impurities was monitored by bolometry and line spectroscopy. No significant impurity production was detected during LH operation, the Z_{eff} value ranging between 1.6 and 2.2. In fig. 6 the time evolution of H_{α}, CIII and BeI is shown during LH modulation. Application of LH power had negligible effect on impurity production.

The central electron temperature was varied from 3 to 11 keV through combined application of LH and ICRH at a power level up to 4.5 MW. The ICRH system was used in monopole configuration in the Hydrogen minority heating scheme with the cyclotron resonance at the plasma centre at 42 MHz. Measurements of the electron temperature profile were obtained through the LIDAR scattering system and Electron Cyclotron Emission diagnostics /9/. The extraordinary mode electron cyclotron emission spectrum was

measured by an absolutely calibrated Michelson interferometer along a sightline perpendicular to the toroidal magnetic field and 13 cm below the equatorial plane. The time resolution of this instrument is ~ 15 ms. ECE measurements with better time resolution (≥ 10 μs) were obtained from a 12 channel grating polychromator giving the time evolution of the electron temperature from the second harmonic extraordinary mode at 12 radial locations in the equatorial plane. Sawtooth activity was monitored by the ECE diagnostics and the soft X-ray SI diode array system /10/, which allows tomographic reconstruction of the X-ray emission up to 20 keV.

Diagnosis of the fast electron population was obtained by a Ge detector PHA system viewing the plasma along a single tangential sightline /11/, capable of measuring continuum X-ray emission up to 250 keV at ~ 100 % efficiency and up to 600 keV with a reduced 10 % detection efficiency, and by a newly developed Fast Electron Bremstrahlung diagnostic /12/ which integrates the X-ray emission along 9 sightlines viewing the plasma poloidally through a 1.5 mm thickness Inconel window installed on a main upper vertical port (fig. 7). Each sightline has a spatial resolution below 15 cm at the plasma midplane and is equipped with CsI (Tl) crystals coupled to Si photodiodes allowing signal detection in up to four energy windows from a low energy limit of 100 keV, determined by detector noise and window transparency. Most of the results so far have been obtained channelling the signal in four 50 KeV energy windows, to an upper energy limit of 300 KeV.

3 - Experimental results

3.1 - Characterization of the fast electron population

Absorption of LH waves into the plasma leads to the development of a high energy parallel streaming electron population. In JET, the LH induced fast electron population have a temperature ≈ 100 keV, of the order of their parallel streaming energy at the Landau damping resonance condition for $n_{\parallel} = 1.8$, and an estimated density production rate ≈ 5 10^{15} m^{-3}/MW at $\bar{n}_e = 2\ 10^{19}$ m^{-3}, corresponding to 0.05 % of the thermal electron density. In fig. 8 the electron bremsstrahlung emission spectrum is shown, as measured by the PHA system.

The ECE spectrum is significantly perturbed by emission from non thermal electrons during LH. Fig. 9a compares the extraordinary mode spectrum from the Michelson interferometer before and during the LH pulse. At low frequencies, normally associated with the first harmonic, fast electrons produce intense relativistically down shifted second harmonic emission which follows closely the LH waveform (fig. 9b). Re-absorption by thermal electrons obscures this emission at higher frequencies (> 125 GHz) where the thermal second harmonic resonance is in the plasma. In the frequency range 125 GHz to ~190 GHz, normally used for electron temperature measurement because the plasma is optically thick to second harmonic radiation, a significant intensity change is also seen. This is mainly due to changes in

electron temperature, but a small contribution from fast electrons radiating down shifted third harmonic emission is be present.

The LH induced perturbation of ECE temperature measurements has been investigated by comparing temperatures measured by the ECE and LIDAR diagnostics. Fig. 10 shows the ratio of electron temperature measured by the LIDAR Thomsom Scattering system to that measured by the ECE system for a large number (~ 300) of LIDAR pulses, versus LH power. To reduce scatter, the temperature profiles from each measurement are averaged over the central 30 cm of the profile, and spurious values with ratios outside the range 0.7 to 1.3 are excluded. Further, each plotted point is an average over 10 observations. A linear regression (solid line) with 95 % confidence intervals (dashed lines) shows a statistically significant trend with LH power. A similar analysis on discharges with and without LHCD shows no statistically significant trends with the main plasma parameters.

The behaviour of LH created fast electrons has also been studied during LH modulation. The time evolution of the 100 % modulated signal measured by the FEB diagnostics is shown in fig. 11 for a central line of sight. At $\bar{n}_e \simeq 1.5\ 10^{19}\ m^{-3}$, the fast electron energy spectrum extends up to 500 keV, reducing to 300 keV at $\bar{n}_e \simeq 2.5\ 10^{19}\ m^{-3}$.

The characteristic rise time τ_R and decay time τ_D of the detected signal are functions of the Landau damping rate, fast electron slowing down time and energy and space diffusion. Fig. 12

shows the variation of τ_R and τ_D with Bremsstrahlung energy and compares it with the fast electron classical slowing down time on the bulk. The $E^{3/2}$ dependence of the slowing down time is in very good agreement with the measurement of τ_R in the 4 energy windows; τ_D on the other hand decreases with increasing energy at a rate which indicates that the electron distribution reaches up to ~ 500 keV. A model is under development to investigate the energy dependence of the diffusion process.

Seven out of the nine sightlines of the FEB diagnostic were used for fast electron profile analysis. The innermost sightline (n. 11 in fig. 7) was not operational during this campaign and the signal measured on the outermost one (n. 19) included a contribution of thick target bremsstrahlung due to fast electrons striking the bottom toroidal belt limiter.

Most of the results have been obtained in limiter plasmas with the plasma centre located between FEB camera channels 15 and 16, as shown in fig. 7. Preliminary results indicate hollow line integrated emission profiles, with hollowness increasing with fast electron energy and bulk electron density (fig. 13). Error bars in the experimental data are mostly due to uncertainties in the detector area exposed to signal collimation. While the density dependence of the profile could be explained in the framework of LH current drive theory, the energy dependence is presently being investigated. A fit to the experimental profile can be achieved using a strongly hollow local emissivity profile peaked at ~ 0.5 m outside the plasma centre, corresponding to a local q value just

below 2. Assuming a smooth variation of the fast electron distribution function with minor radius, the good agreement shown in fig. 13 indicates a hollow density profile of the non inductive current carrying fast electrons.

3.2 - Current Drive efficiency

Estimation of the LHCD efficiency $\gamma = \bar{n}_e I_{CD} R / P_{LH}$, where I_{CD} is the non inductively driven current, R the plasma major radius and P_{LH} the LH power, is based upon analysis of the measured surface loop voltage. Up to 50 % drop in loop voltage is observed (fig. 14) at $P_{LH}/\bar{n}_e \sim 0.6\ 10^{-19}$ MW m^3, with no noticeable dependence on the feedback controlled total plasma current. In these conditions up to 3 Vs of resistive flux are saved, corresponding to ~ 30 % of the overall resistive flux consumption during the current flat top (fig. 15). No attempt has yet been made to optimize Volt second savings, for instance applying LH during the current rise phase.

Current Drive efficiency depends upon the launched $n_\parallel$ spectrum, as suggested by theory /13/ and observed in many experiments. Phasing between klystrons is optimized in JET by monitoring the cross talk between adiacent multijunctions and the coupling to the plasma. In fig. 16 the normalized loop voltage reduction during LH is shown as a function of klystron phasing. The broad maximum below 0° corresponds to a peak $n_\parallel \sim 1.6$. Most of the experimental campaign has been carried out at 0° phasing between multijunctions, corresponding to $n_\parallel = 1.8$.

As already reported by JT-60, γ depends on Z_{eff} and the volume averaged electron temperature $\langle T_e \rangle$, as shown in fig. 17. The LH driven current is computed by taking into account the time behaviour of the internal inductance and changes in Z_{eff} and T_e. The additional effect of the residual electric field on the LH fast electrons is estimated in the first order in the electric field /14/ and is found to be less than 20 % of the total driven current in most cases. At $\langle T_e \rangle \sim 1.9$ keV and $\bar{n}_e \simeq 2\ 10^{19} m^{-3}$, $\gamma \sim 0.4\ 10^{20} m^{-2} A/W$, corresponding to ≤ 1.2 MA non inductive current. The strong temperature dependence of the efficiency is in qualitative agreement with the spectral gap model where the energy required to fill in the gap in velocity space is reduced when the electron temperature increases. In JET, γ follows approximately the empirical JT-60 scaling law and reaches the maximum value predicted by Fisch's theory. One of the objectives of the next campaign will be to investigate whether a saturation of γ occurs at higher $\langle T_e \rangle$ values.

3.3 - Current profile effects

Typical time evolution of the internal inductance l_i, with and without ICRH, is shown in fig. 18. LH application during the ohmic phase leads to current profile broadening with a decrease of l_i, eventually reaching a steady state after ~ 8 sec, comparable with the current diffusion time. When LH is applied in conjunction with ICRH, the current broadening compensates the peaking due to central electron heating. This effect is highlighted in fig. 19,

where the power waveforms of LH and ICRH are shown together with the time evolution of the internal inductance for three successive discharges. Application of 1.5 MW of LH to an ICRF heated 2 MA limiter discharge leads to a broadening of the current density profile, with $l_i \sim 1.10$ (fig. 19b(2)) in contrast to the case of ICRH alone where $l_i \sim 1.17$ (fig. 19b(1)). The current profile control is lost on a current diffusion time scale when the LH power is replaced by ICRH alone (fig. 19b(3)).

The current profile broadening is also evident in fig. 20, where radial profiles of the safety factor q, as determined by equilibrium analysis of the magnetic signals, are shown with and without LHCD and compared with the sawtooth inversion radius as determined from soft x-ray measurements. The 10 % rise in central q is in agreement with indications of peripheral absorption of Lower Hybrid waves obtained from ray tracing and Fokker-Planck computations /15/.

3.4 - Sawtooth stabilization and electron heating

Long sawtooth free periods of the "monster" type have been achieved in ICRF heated plasmas, up to 2.9 sec at 2 MA of plasma current and 2.3 sec at 3 MA. Fig. 21 shows the time evolution of the central electron temperature, as measured by the ECE Fabry-Perot Interferometer. Long sawtooth free periods are obtained when LH power in excess of 1 MW is coupled to the plasma. In these conditions, the power threshold for sawtooth stabilization for periods in excess of the plasma energy

confinement time with ICRH alone is ≃ 5 MW /16/. This result is further supported by a statistical analysis carried out on a subset of discharges with similar plasma conditions but different LH and ICRH power levels, which shows that combined LH and ICRH operation leads to substantial lengthening of the sawtooth free period (fig. 22). In the particular case of fig. 21b, the "monster" sawtooth terminates due to a continuous density increase throughout the pulse. The lowering of the sawtooth stabilization ICRH power threshold could be explained by a combination of stabilization effects due to fast minority ions accelerated by ICRH and reduction of the q = 1 surface volume due to off-axis LHCD.

Substantial central electron heating is observed during application of LH power on JET (fig. 23). The central electron heating efficiency is ≃ 0.5 keV/MW with LH alone, rising to values of the order of 1.0 keV/MW during combined LH and ICRH (fig.24). The local power deposition on the bulk electrons was estimated by using the change of slope of the electron temperature during the LH power modulation phase, as measured by the Fabry-Perot Interferometer, under the assumption that confinement and power input terms, other than LH, remain unchanged (fig. 25). This hypothesis is supported by the fact that no modification of the m=1 activity level is detected when LH is applied and by the observed delayed response of the surface loop voltage. The modulated power deposition profile, deduced during LH power modulation, is shown in fig. 26, for two typical cases with and without ICRH.

This result, in particular the higher heating rate during combined LHCD and ICRH, is in apparent conflict with the already reported profile hollowness of the current carrying fast electrons. It must be observed however that the increase in hollowness with increasing fast electron energy, as measured by the FEB diagnostic in the range 100 keV to 300 keV, could indicate progressively shallower profiles for lower energy fast electrons, possibly due to an inward diffusion process. In this case electrons with few tens of keV might be present at the plasma centre, thus improving the TTMP damping of the fast magnetosonic ion cyclotron wave, leading to more efficient central electron heating /17/. Moreover, as LH driven fast electrons are preferentially distributed in the forward velocity direction, TTMP damping will be asymmetric in parallel velocity, thus contributing to the current drive mechanism. The electron power deposition profiles shown in fig. 26 indicate that ~ 400 kW, corresponding to ~ 10 % of the ICRH power, are transferred to the fast electron population. Including this power reduces the estimate of the current drive efficiency to $\gamma \sim 0.32\ 10^{20}\ m^{-2}A/W$.

4 - Conclusions and further developments

The JET LHCD system has successfully started operation during the 1990 experimental campaign, coupling up 1.7 MW of power into different plasma scenarios.

Current Drive efficiencies up to $0.4\ 10^{20}m^{-2}$ A/W at $\langle T_e \rangle$ =

1.9 keV and $\bar{n}_e = 2\ 10^{19}\ m^{-3}$ and a degree of control of the current density profile have been achieved with a high directivity narrow spectrum of lower hybrid waves at 3.7 GHz, coupled to the plasma through a multijunction type launcher. The temperature scaling of the CD efficiency, already observed in JT-60, has been confirmed in the temperature range 0.9 keV $\leq \langle T_e \rangle \leq$ 1.9 keV.

LH operation in 2 and 3 MA ICRF heated plasmas has led to sawtooth free periods up to 2.3 and 2.9 sec. Central electron heating at a rate of 0.5 keV/MW and 1 keV/MW has been observed in Ohmic and ICRH plasmas respectively.

Substantial bremsstrahlung emission is observed during LH, corresponding to fast electron energies up to 300 keV at $\bar{n}_e = 2.5\ 10^{19}\ m^{-3}$. The upper energy limit increases with decreasing density of the bulk electrons. Hollow emissivity profiles have been measured, the profile hollowness increasing with electron density and fast electron energy. The dependence on electron density is in qualitative agreement with ray tracing calculations. However, the penetration of fast electrons is found to be deeper that code predictions.

The observations of central electron heating and hollow fast electron source appear in conflict which each other. Inward diffusion of lower energy fast electrons might eventually lead to synergism between TTMP and LH wave damping.

The full LHCD system, capable of launching 12 MW of LH power,

will be operational during the Divertor phase of JET, foreseen after 1992.

Acknowledgements

We gratefully acknowledge the continuous effort of the whole JET team during the experimental campaign, in particular our colleagues responsible for diagnostic, ICRF plant operation and machine operation, including our colleagues from AEA, CEA and ENEA Associations working at JET under Task Agreement contracts.

We also acknowledge fruitful discussions with P.H. Rebut, D. Start, Y. Peysson and the LHCD team on Tore Supra.

References

/1/ - J.E. Stevens, R.E. Bell, S. Bernabei et al., Nucl. Fus. **28** (1988) 217.

/2/ - F.X. Söldner,F. Leuterer, M. Brambilla et al., Proc. of the 13th IAEA International Conference on Plasma Physics and Controlled Nuclear Fusion Research, Washington DC, USA, 1-6 October 1990.

/3/ - C. Gormezano, P. Briand, G. Briffod et al., Nucl. Fus. **25** (1985) 4.

M. Nagami and the JT-60 Team, Proc. of the 13th IAEA International Conference on Plasma Physics and Controlled Nuclear Fusion Research, Washington DC, USA, 1-6 October 1990.

T. Imai, H. Kimura, Y. Kusama et al., ibidem.

/4/ - P.H. Rebut and the JET Team, Proc. of the 13th IAEA International Conference on Plasma Physics and Controlled Nuclear Fusion Research, Washington DC, USA, 1-6 October 1990.

/5/ - M. Pain, H. Brinkschulte, G. Bosia et al., Proceedings of 13th Symp. on Fus. Eng., Knoxville (Te), USA, 1989.

/6/ - M. Brusati, J.P. Christiansen, J.G. Cordey, K. Jarrett, E. Lazzaro, R.T. Ross, Comp. Phys. Rep., **1** (1984) 345.

/7/ - G. Braithwaite, N. Gottardi, G. Magyar, J. O'Rourke, J. Ryan, D. Veron, Rev. Sci. Instrum., **60** (1989) 2825.

/8/ - H. Saltzmann, J. Bundgaard, A. Gadd et al., Rev. Sci. Instrum., **59** (1988) 1451.

/9/ - D.V. Bartlett, D.J. Campbell, A.E. Costley et al., Proceedings of the 6th Joint Workshop on ECE and ECRH, CLM-ECR (1987), Oxford, September 1987.

/10/ - A. W. Edwards, H-U Fahrbach, R.D. Gill et al., Rev Sci. Instrum., **57** (1986) 2141.

/11/ - D. Pasini, R.D. Gill, J. Holm, E. Van Der Goot, A. Weller, Rev. Sci. Instrum., **59** (1988) 693.

/12/ - P. Froissard, M. Adams, M. Brusati et al., Proc. 18th EPS Conference on Controlled Fusion and Plasma Physics, Berlin (Germany), 3-7 June 1991.

/13/ - N. Fisch, Rev. Mod. Phys., **59** (1987) 175.

/14/ - N. Fisch, Phys. of Fluids, **28** (1985) 245.

/15/ - M. Brusati, C. Gormezano, S Knowlton, M. Lorentz-Gottardi, F. Rimini, Proc. 8th Top. Conf. on Radio Frequency Power in Plasmas, Irvine (Ca), 1989.

/16/ - D.J. Campbell, D.F.H. Start, J. Wesson et al., Phys. Rev. Lett., **21** (1988) 2148.

/17/ - J. Jacquinot and the JET Team, invited paper at the 18th EPS Conference on Controlled Fusion and Plasma Physics, Berlin (Germany), 3-7 June 1991.

D. Moreau and C Gormezano, invited paper at the 18th EPS Conference on Controlled Fusion and Plasma Physics, Berlin (Germany), 3-7 June 1991.

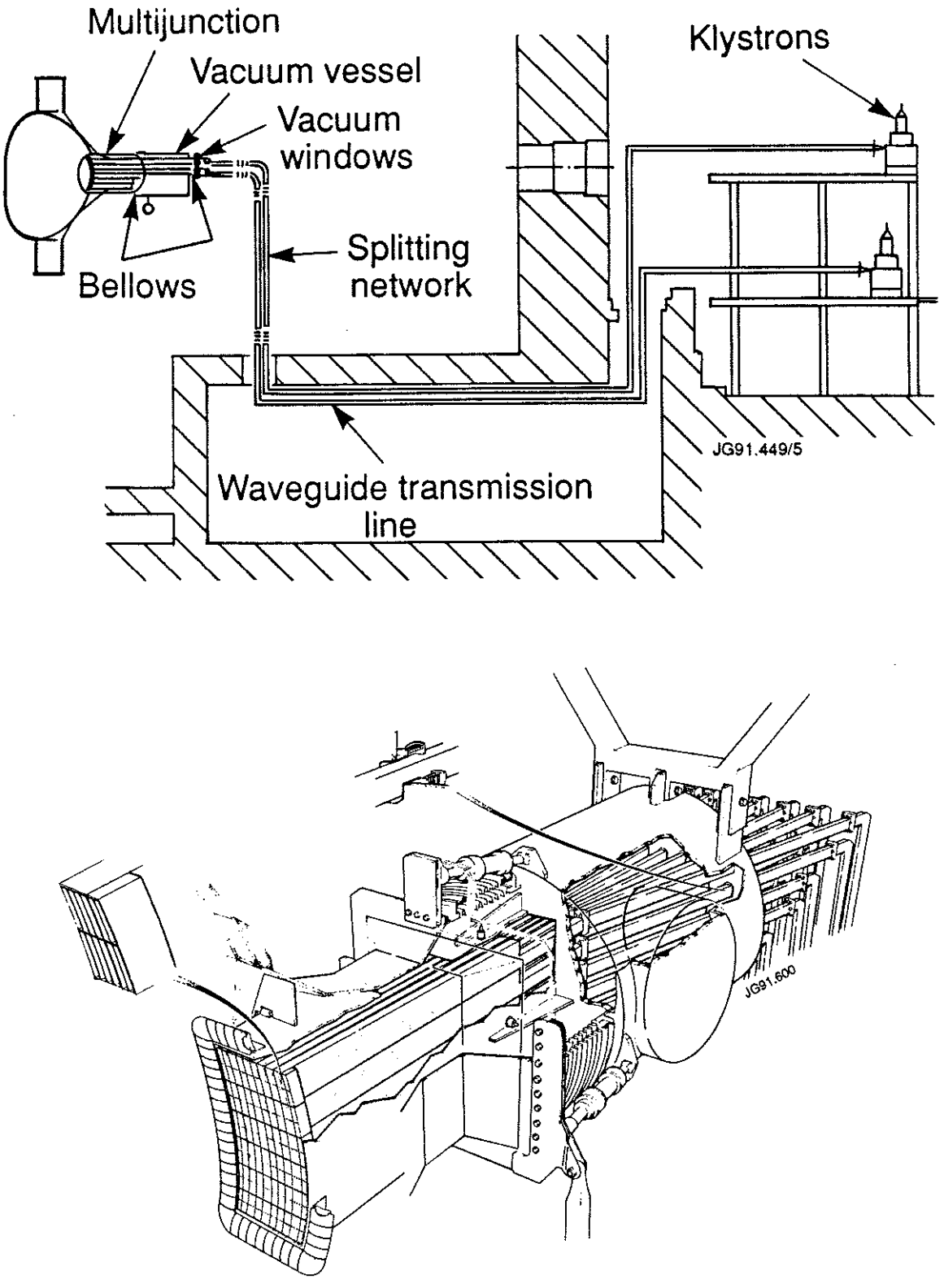

fig. 1 - Schematic layout of the JET Lower Hybrid prototype system. (Top) side view of the LHCD plant. The waveguide transmission line is oversized up to the Splitting Network and measures approximately 40 m in length. (Bottom) general view of the JET multijunction type launcher.

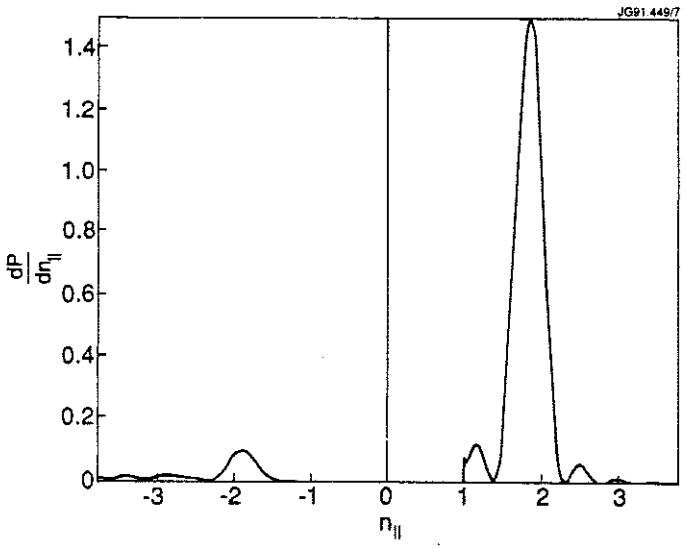

fig. 2 - Normalized Lower Hybrid power spectrum for 0° phasing between klystrons, for the LHCD prototype system.

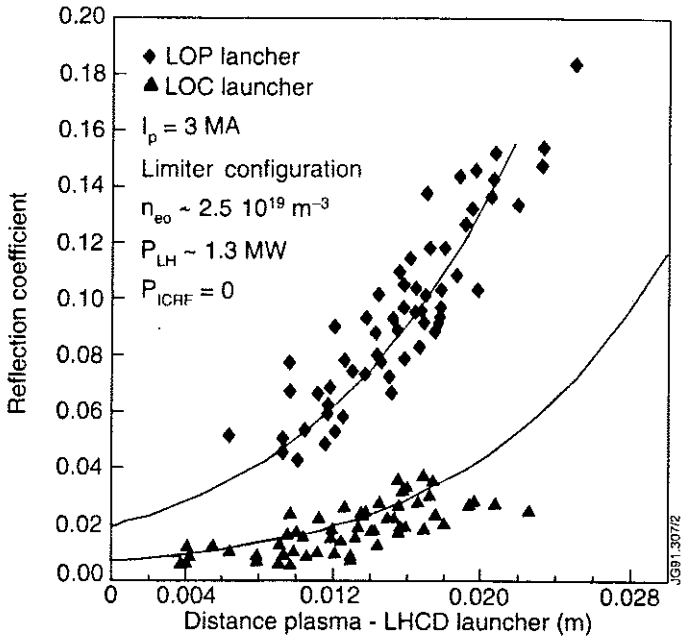

fig. 3 - Power reflection coefficient vs. plasma-launcher distance for the Cadarache (LOC - upper half) and JET (LOP - lower half) multijunctions. The plasma - launcher distance refers to the protection tiles at the launcher midplane. The difference in reflection coefficient between the two types of multijunctions is explained by the fact that LOC is ~ 3 mm behind the tiles, while LOP is 5 mm further away.

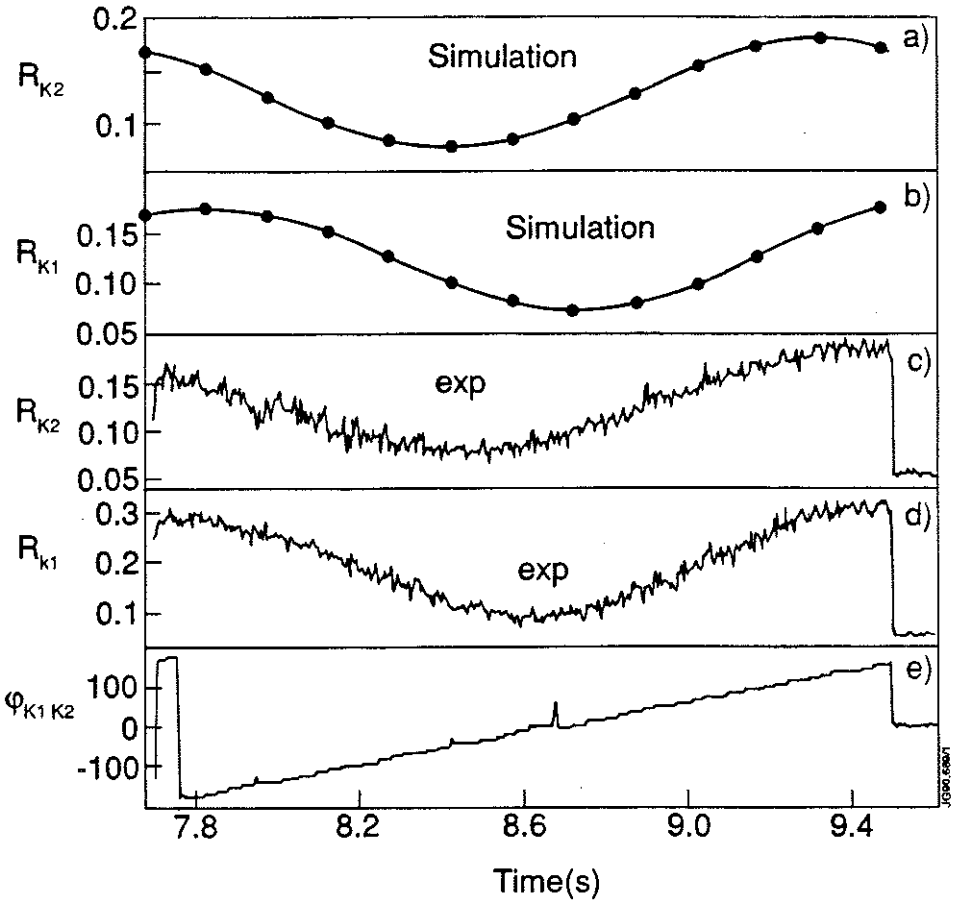

fig. 4 - Phase measurements at the grill mouth between two multijunctions: (a,b) code simulation of the reflection coefficient on two neighbouring waveguides, (c,d) corresponding experimental value of the reflection coefficient, (e) phase waveform applied between the multijunctions.

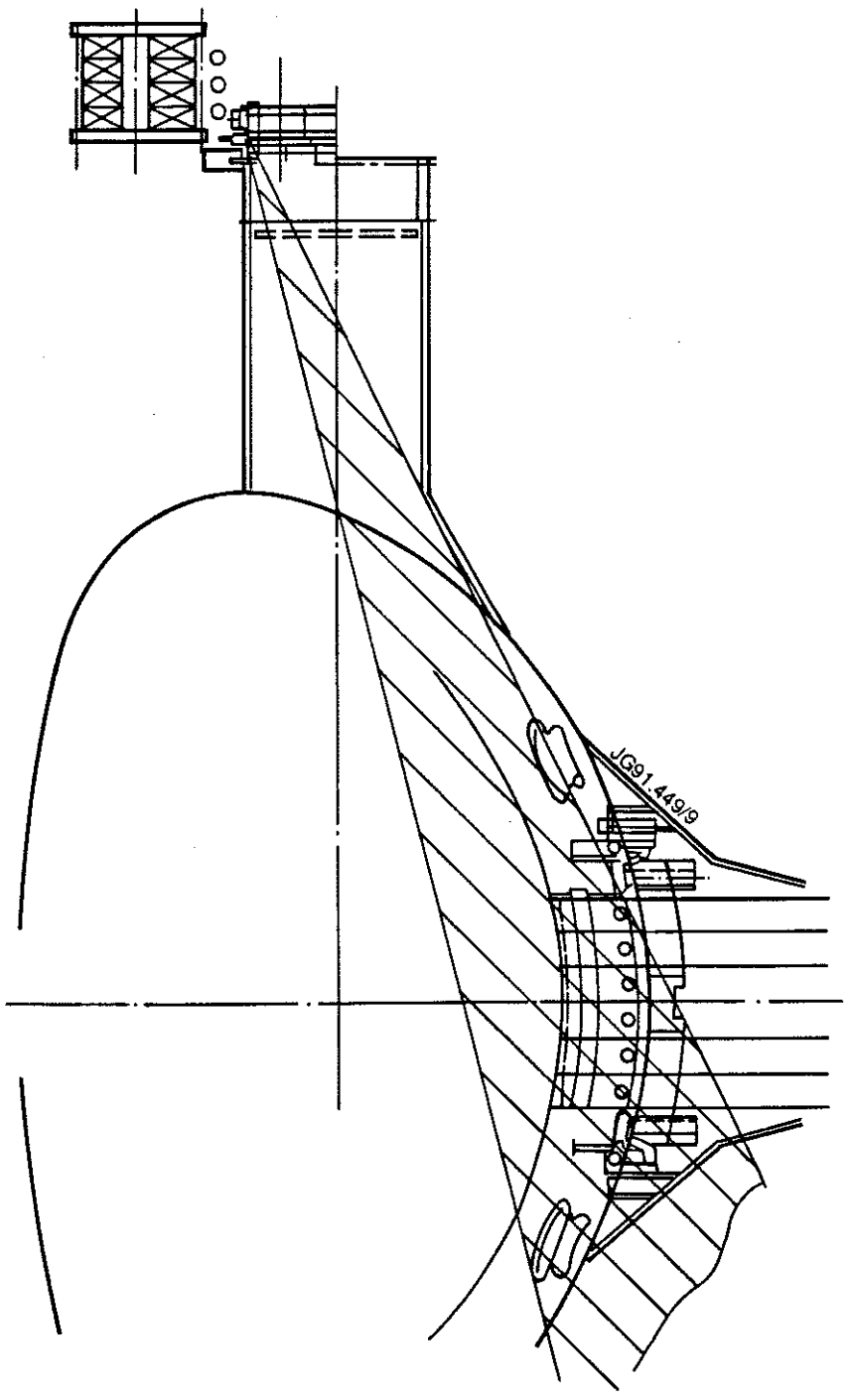

fig. 5 - Side view of the CCD camera launcher viewing system. This system allows viewing of top and bottom toroidal belt Beryllium limiters, for a total extent of ~ 300 mm, due to the viewing access of the vertical port.

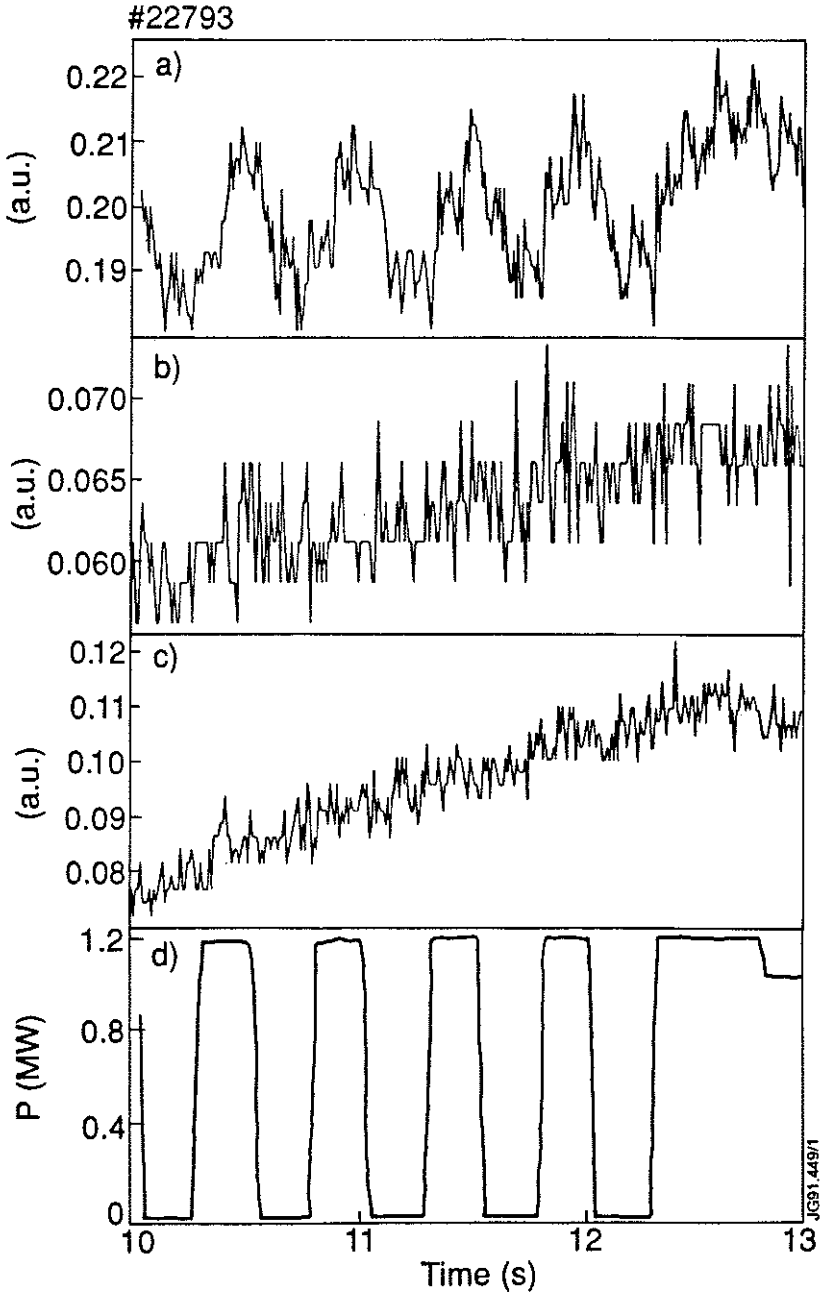

fig. 6 - Time evolution of (a) H_α, (b) CIII line and (c) BeI line during (d) LH power modulation. Impurity production during LH does not differ from that observed during Ohmic plasmas.

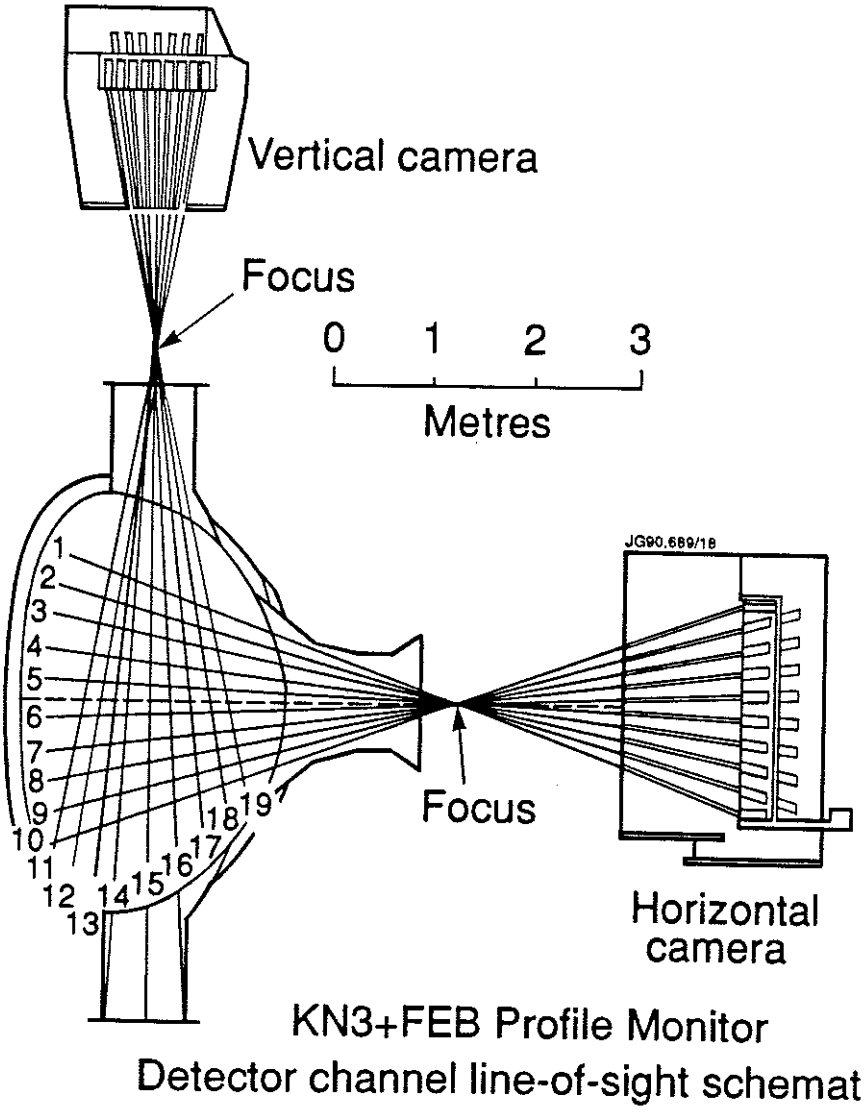

fig. 7 - Viewing geometry of the FEB diagnostic. Only the vertical FEB camera was operational during the campaign. The signal on channel 19 is affected by γ emission from the bottom belt limiter.

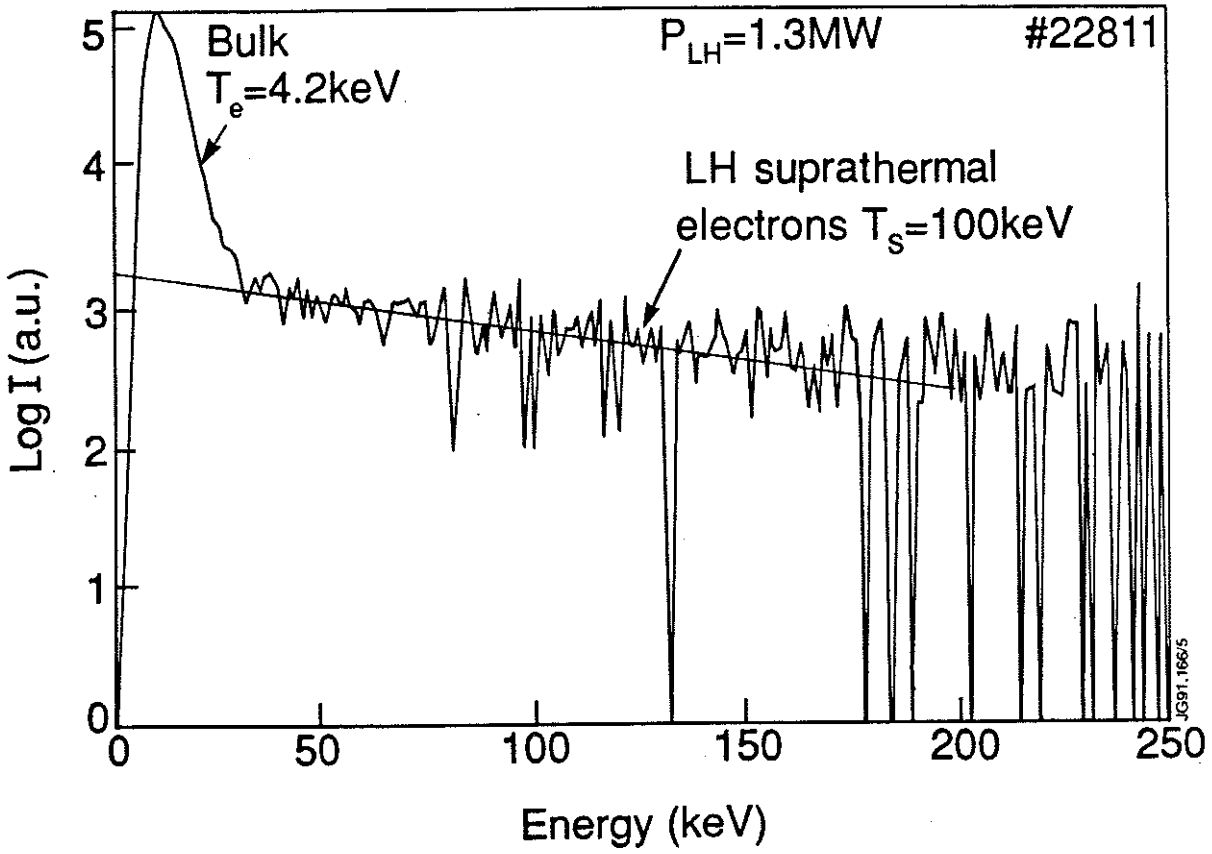

fig. 8 - Forward electron bremsstrahlung emission spectrum, as measured by the tangential viewing PHA system, for P_{LH} = 1.3 MW and $\bar{n}_e \simeq 2\ 10^{19}\ m^{-3}$.

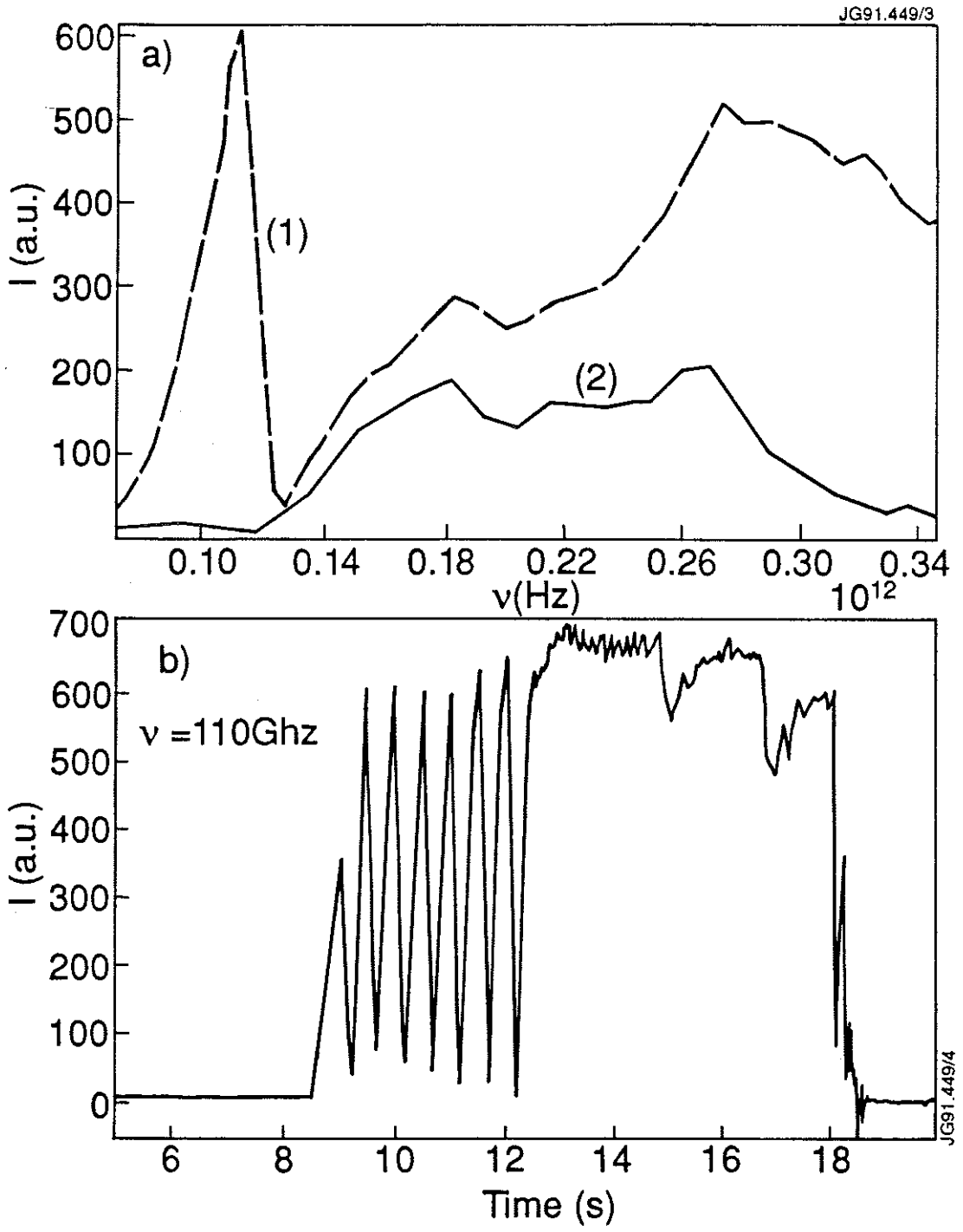

fig. 9 - Non-thermal Electron Cyclotron Emission during LH. (a) Calibrated frequency spectrum with (--) and without (—) LH. The high frequency shoulder above 110 GHz is due to plasma reabsorption. (b) Time evolution of the intensity at 110 GHz during LH modulation. The fast decay time (≈ 15 ms) is consistent with peripheral emission.

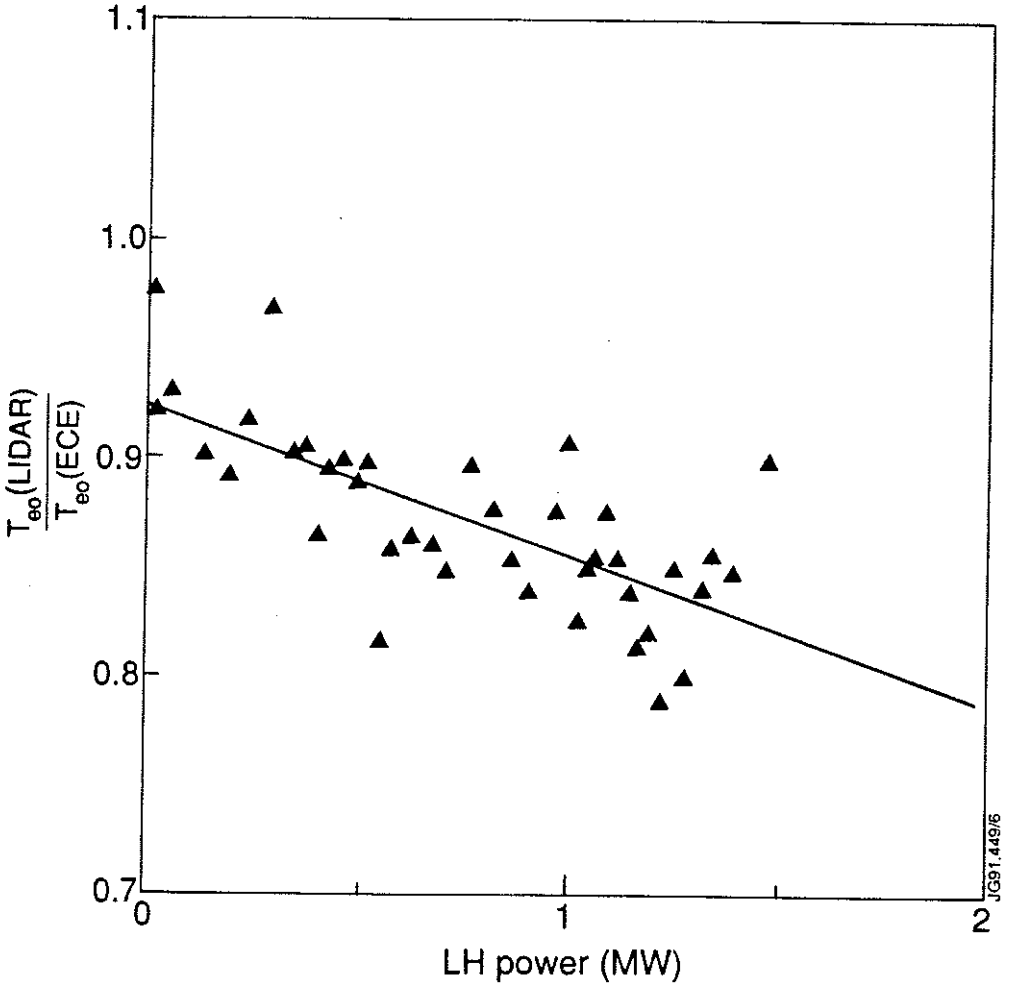

fig.10 - LIDAR to ECE measured central electron temperature vs. LH power. Each point represents an average of ten measurements.

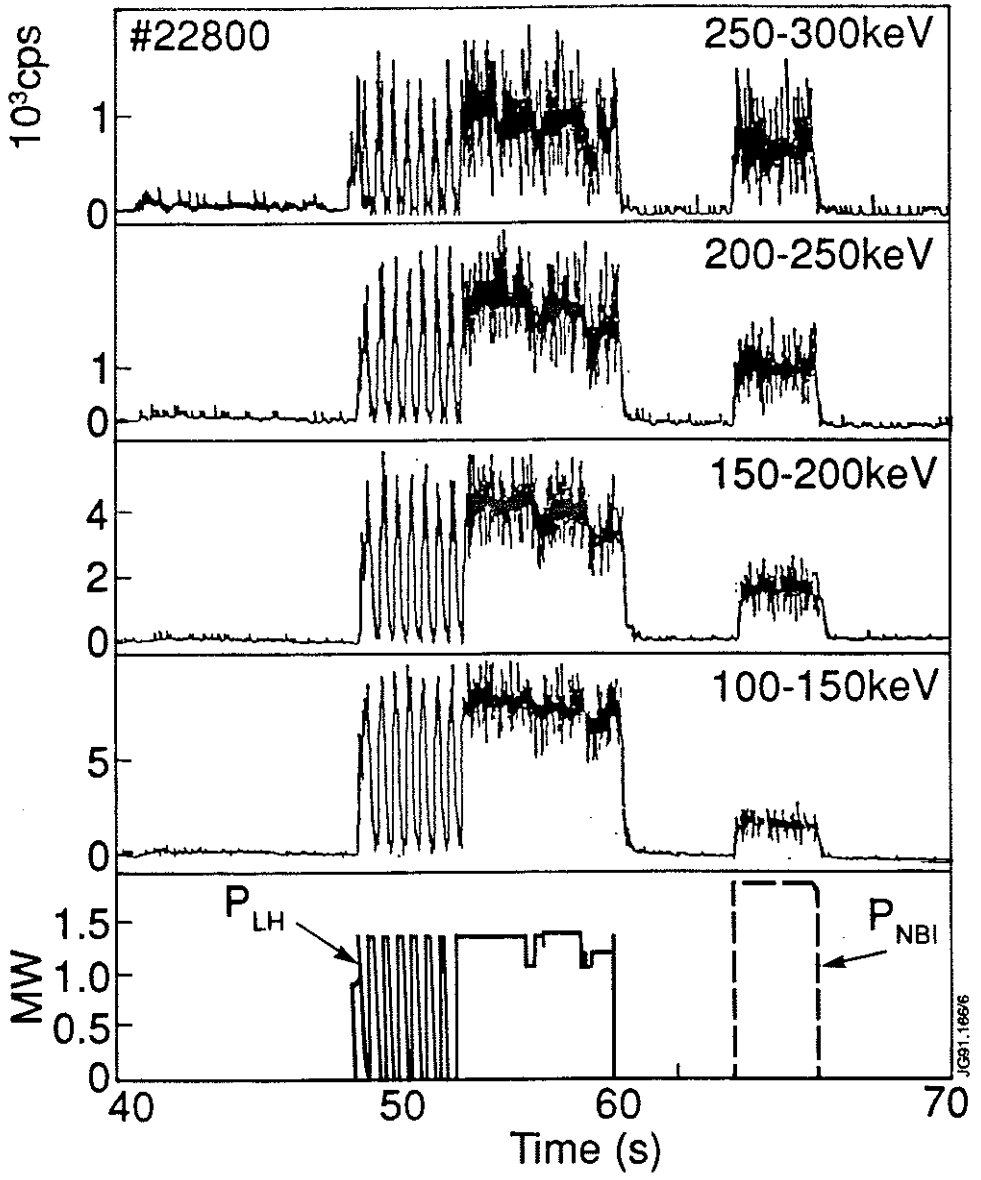

fig. 11 - Time evolution of FEB signal in the four energy windows. The signal detected during Neutral Beam Injection is neutron induced.

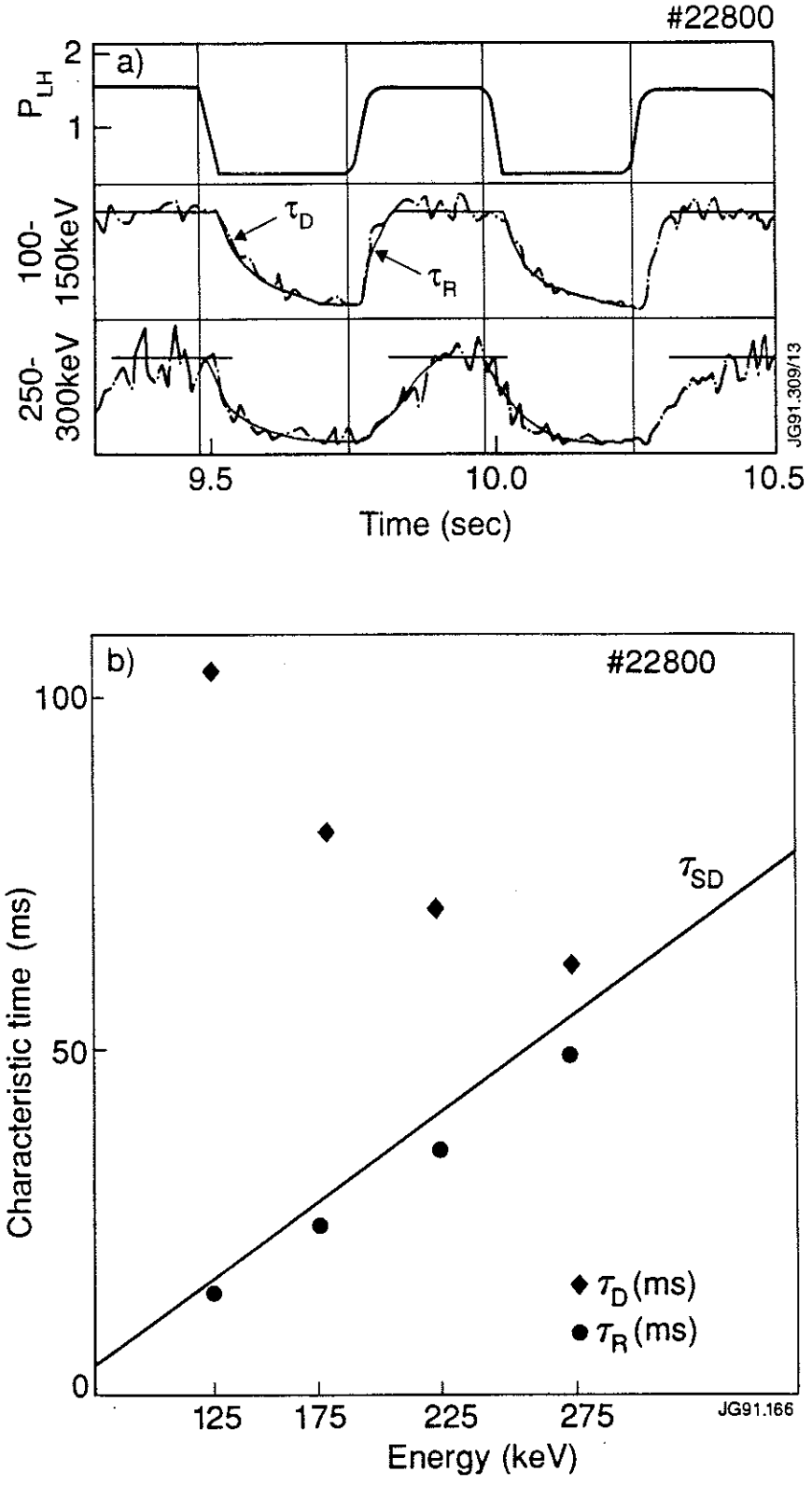

fig. 12 - a) Time evolution of the FEB signal during LH modulation. b) Rise (•) and decay (■) times τ_R and τ_D of the FEB emission signal during LH modulation, as a function of $E^{3/2}$. The slowing down time τ_{SD}(—) is computed assuming fast electron-thermal electron collisions.

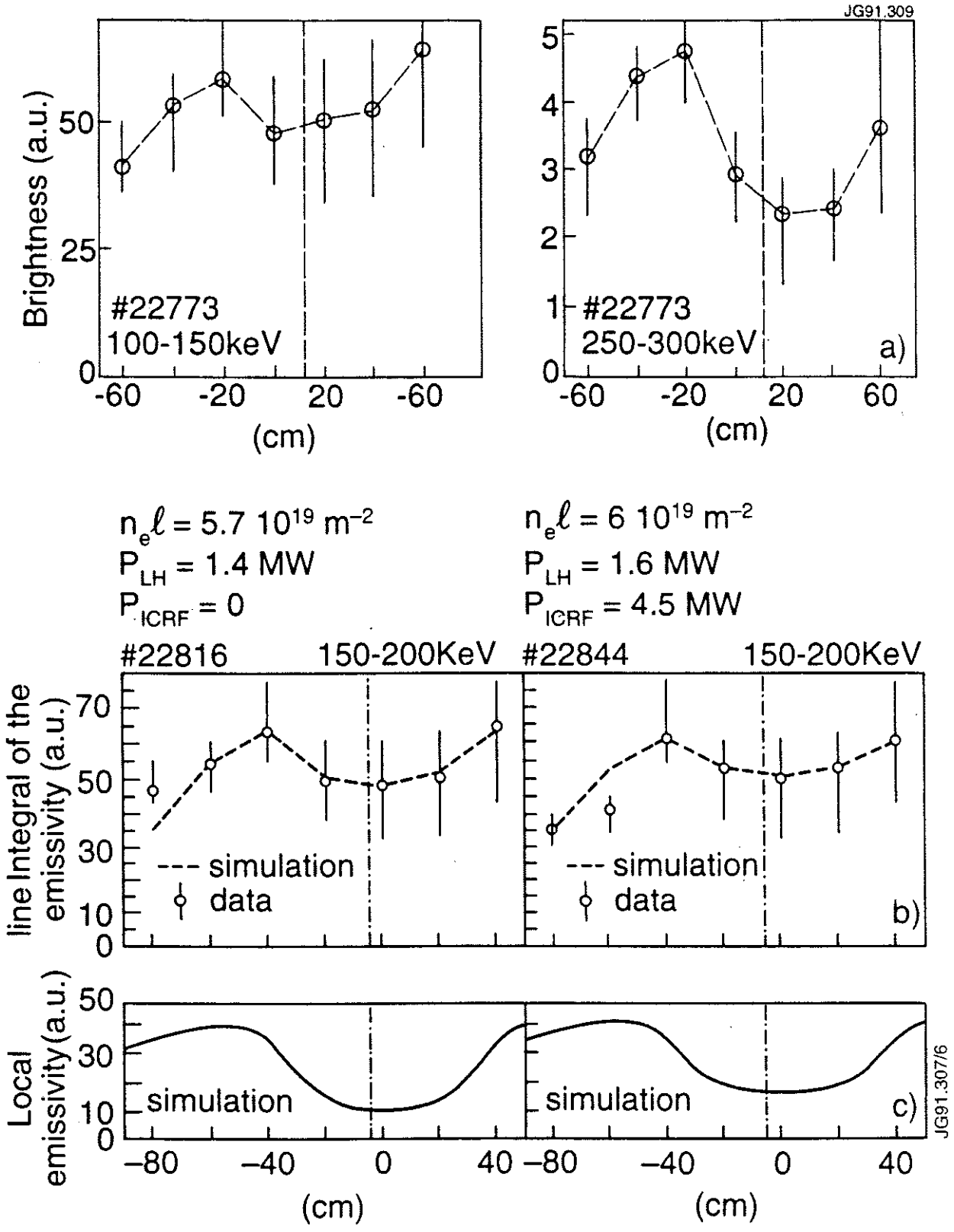

fig.13 - Evolution of the FEB brightness profile with photon energy (a) and thermal electron density (b). The fit to the experimental data points in (b) is computed assuming the hollow emissivity profile shown in (c). The dashed vertical line indicate the position of the plasma centre.

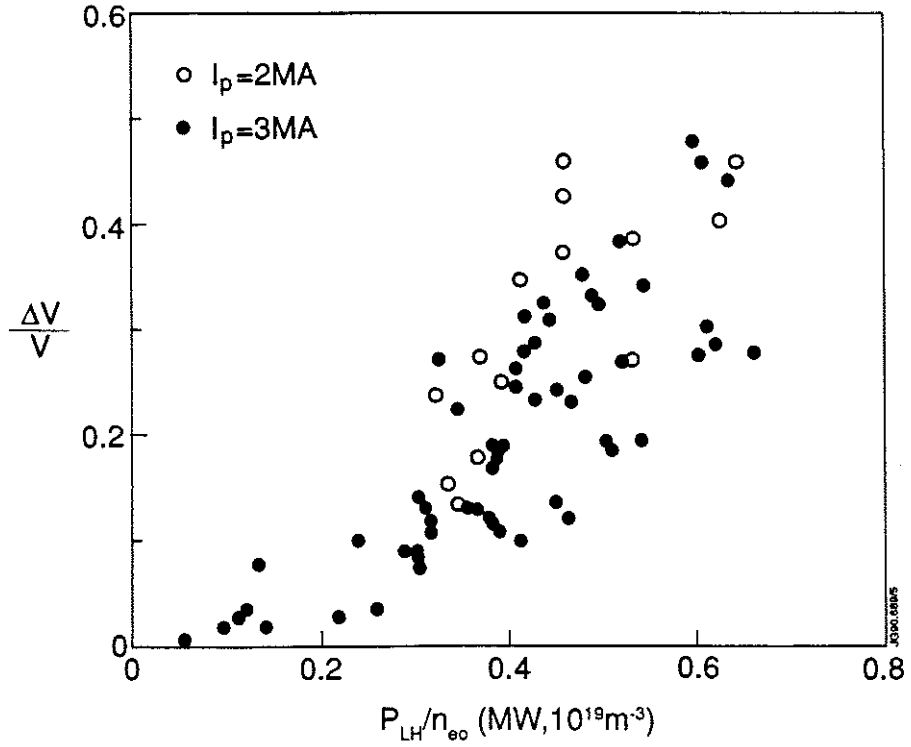

fig.14 - Relative change of loop voltage vs. the LH power per particle parameter, at 2 and 3 MA. All data points refer to steady state conditions.

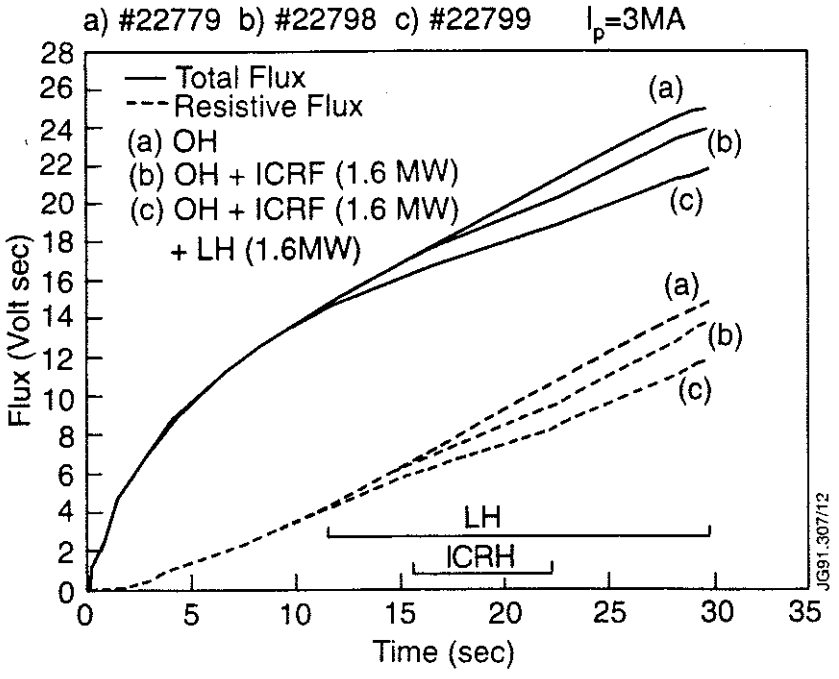

fig.15 - Flux consumption during LH, ICRH. The lower resistivity during electron heating by ICRH accounts for 30 % of the overall Volt seconds savings.

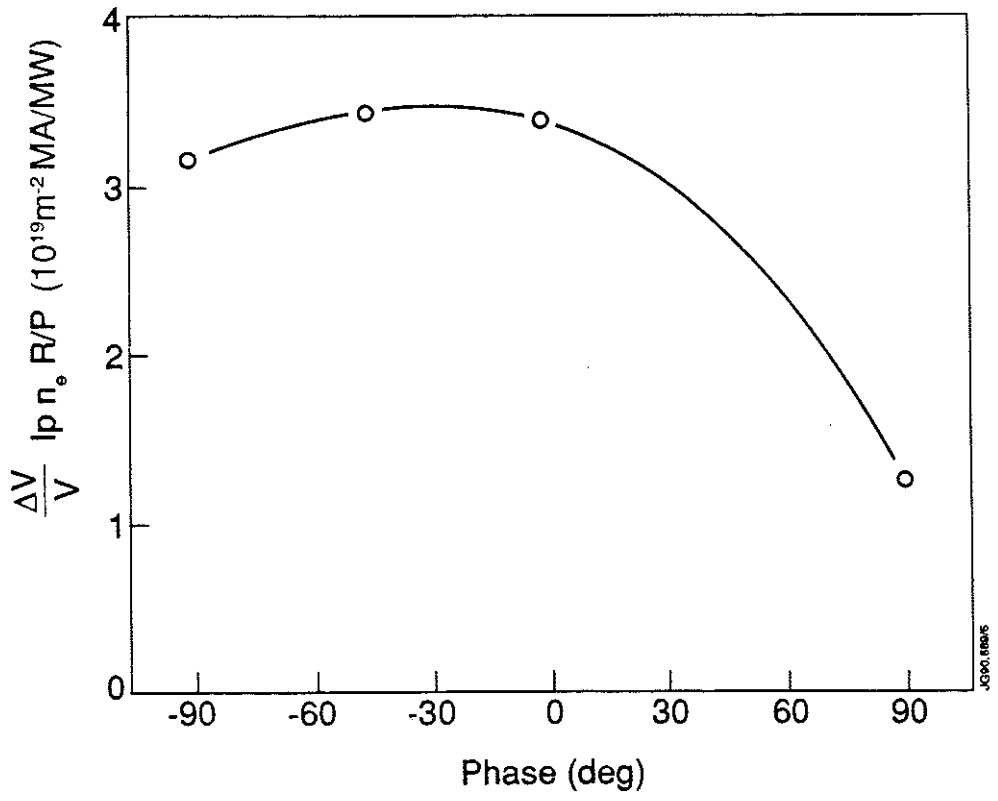

fig. 16 - Normalized loop voltage drop during LH operation vs. the klystron phasing.

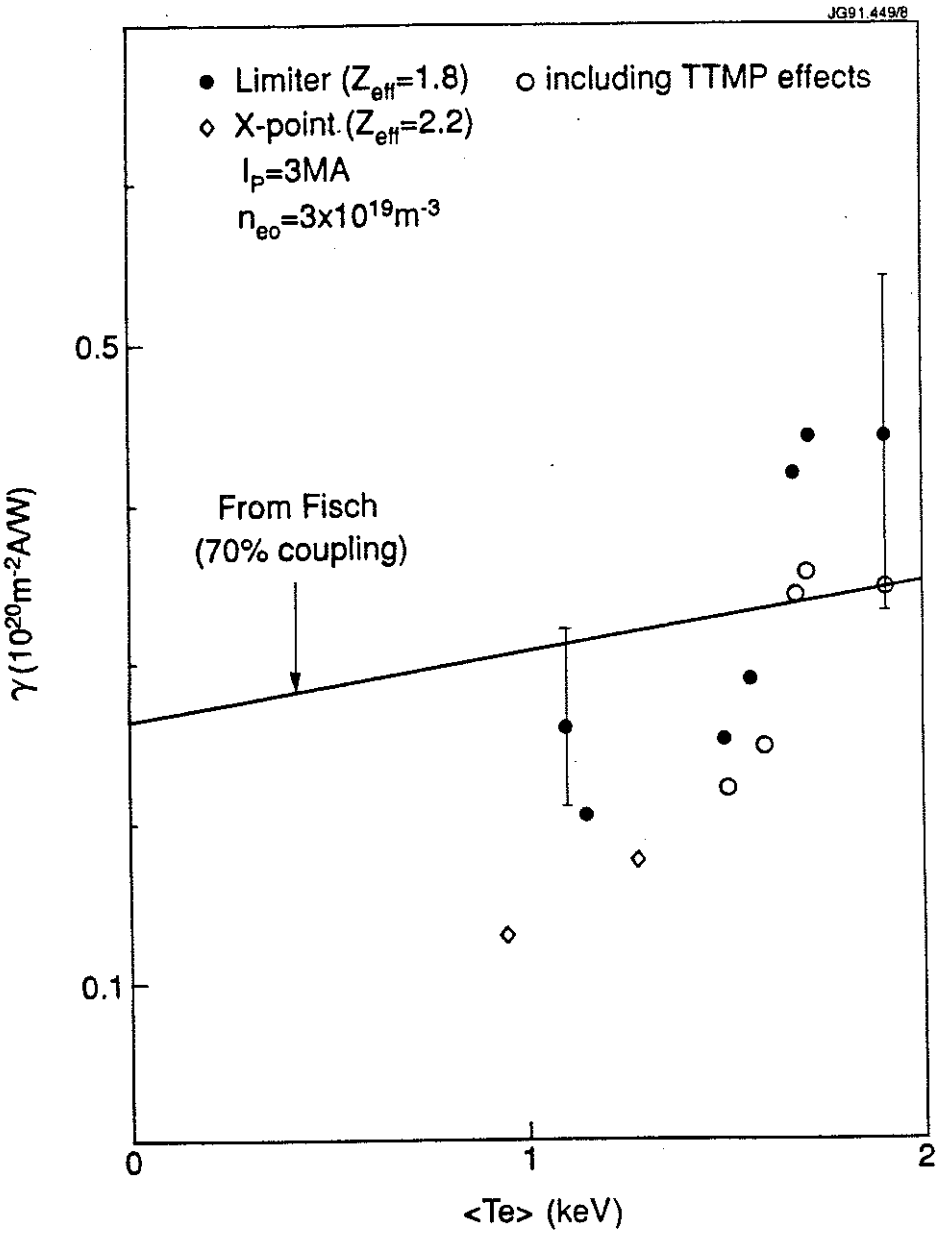

fig. 17 - LH current drive efficiency γ vs. volume average electron temperature $\langle T_e \rangle$. The open circles are computed taken into account ~ 400 kW of FWCD.

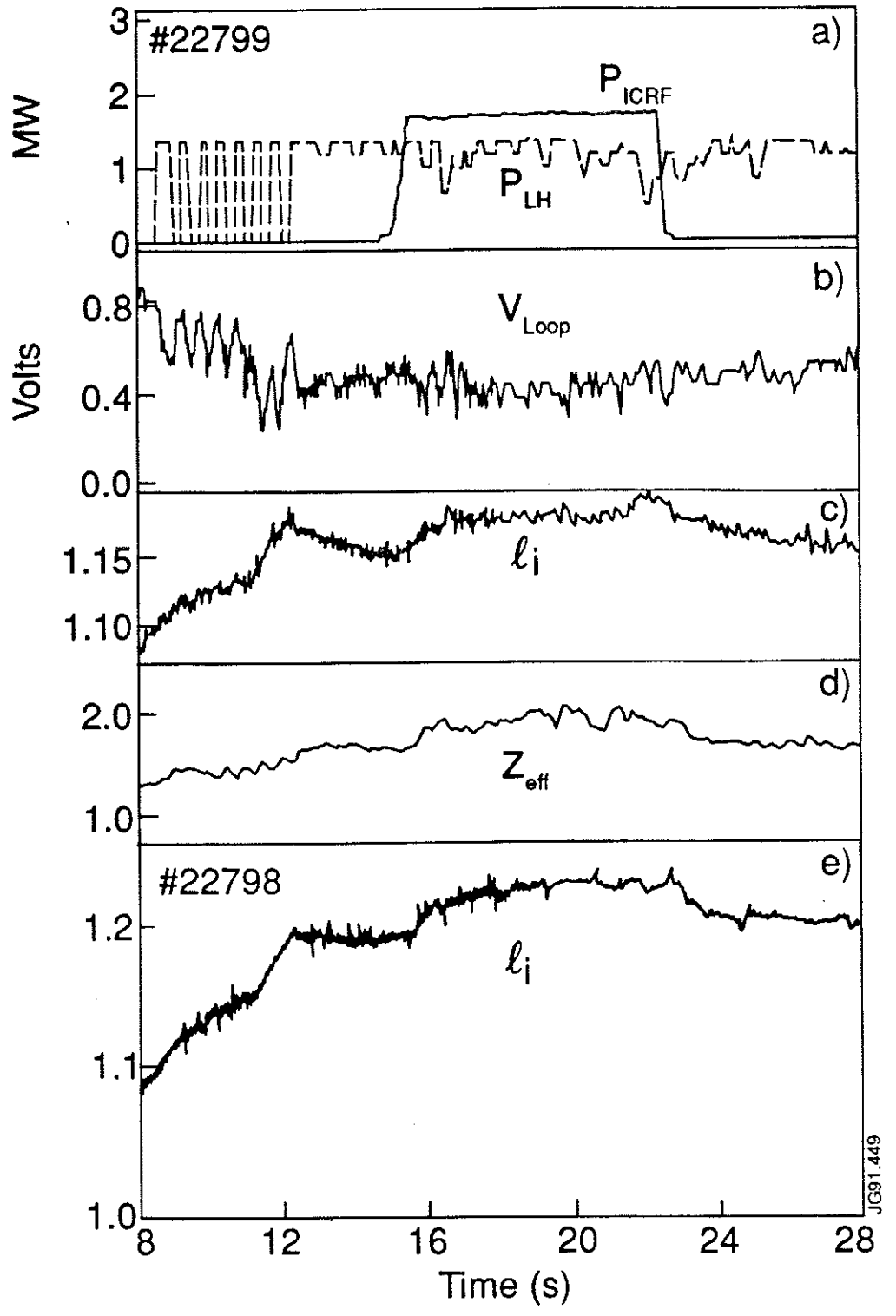

fig.18 - Time evolution of LH, ICRH power (a), surface loop voltage (b), internal inductance l_i (c) and Z_{eff} (d), in a 3 MA, 2.8 T limiter discharge. The behaviour of the internal inductance in a reference discharge without LH is shown in (e).

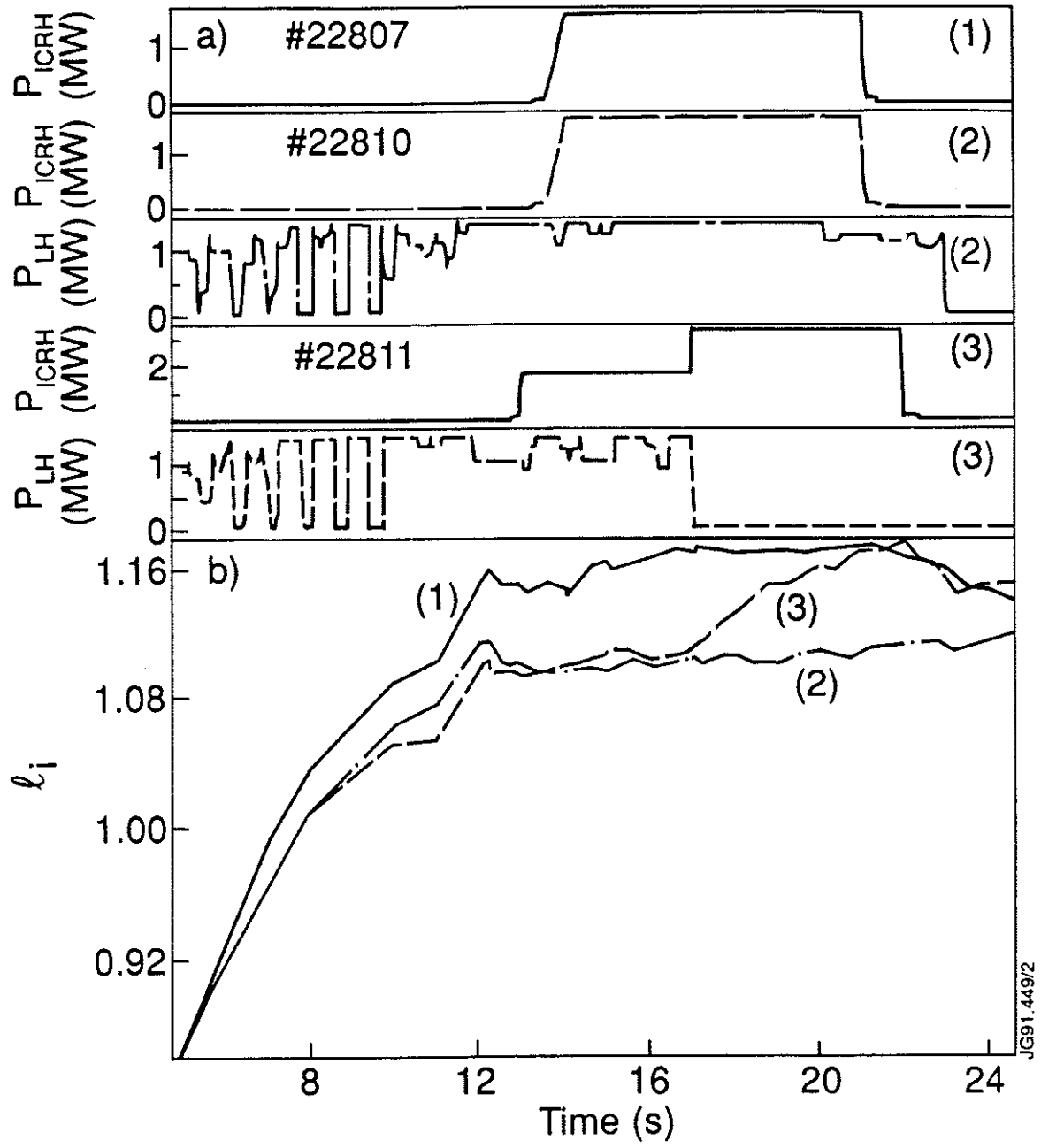

fig.19 - Power waveforms (a) and time evolution of the internal inductance (b) in LH, ICRH discharges: (1) ICRH alone, (2) ICRH + LH, (3) effect on l_i of replacing LH with ICRH power at t = 17 sec.

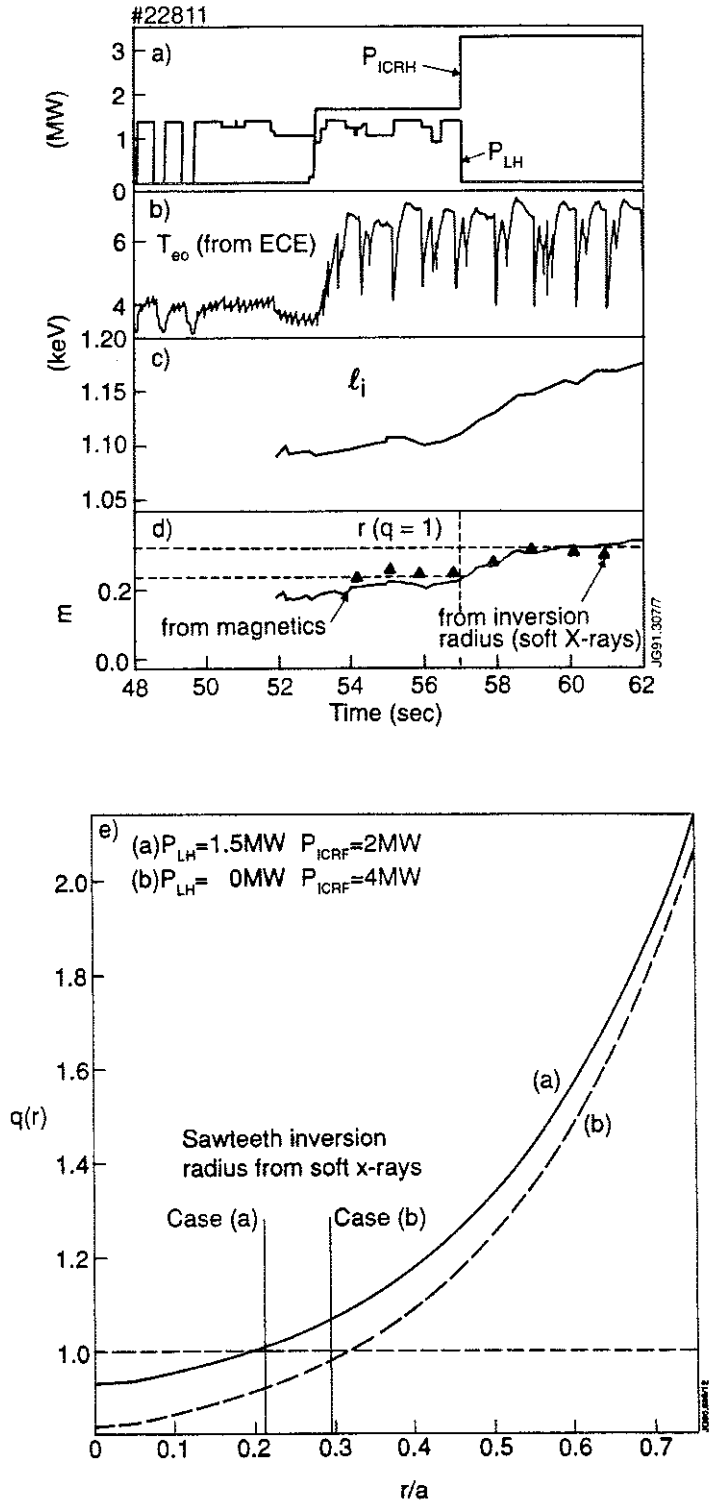

fig.20 - Time evolution of (a) LH and ICRH power, (b) central electron temperature, (c) internal plasma inductance and (d) radial position of q=1 and inversion radius surfaces. (e) Radial profile of the safety factor q with and without LHCD as deduced from IDENTC, compared with sawtooth inversion radius as measured from the soft x-ray diode array.

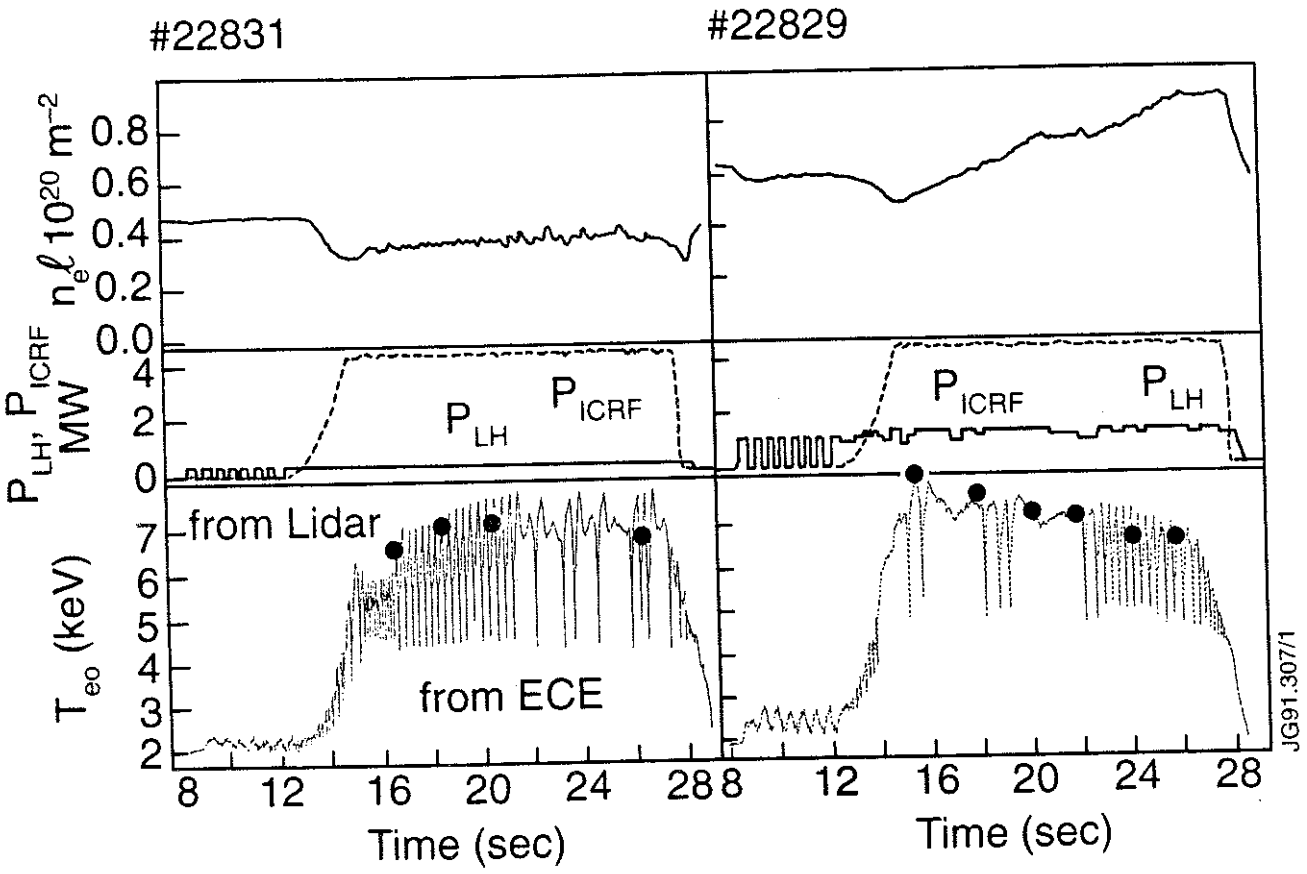

fig.21 - Time evolution of the central electron temperature, as measured by the ECE Michelson Interferometer (—) and the LIDAR diagnostic (•), without (left, pulse # 22831) and with (right, pulse # 22829) LH. The top traces show the time evolution of the line integrated electron density. The lack of sawtooth stabilization after 22 sec on pulse 22829 is due to worsening of the LH coupling, due to the density buid-up.

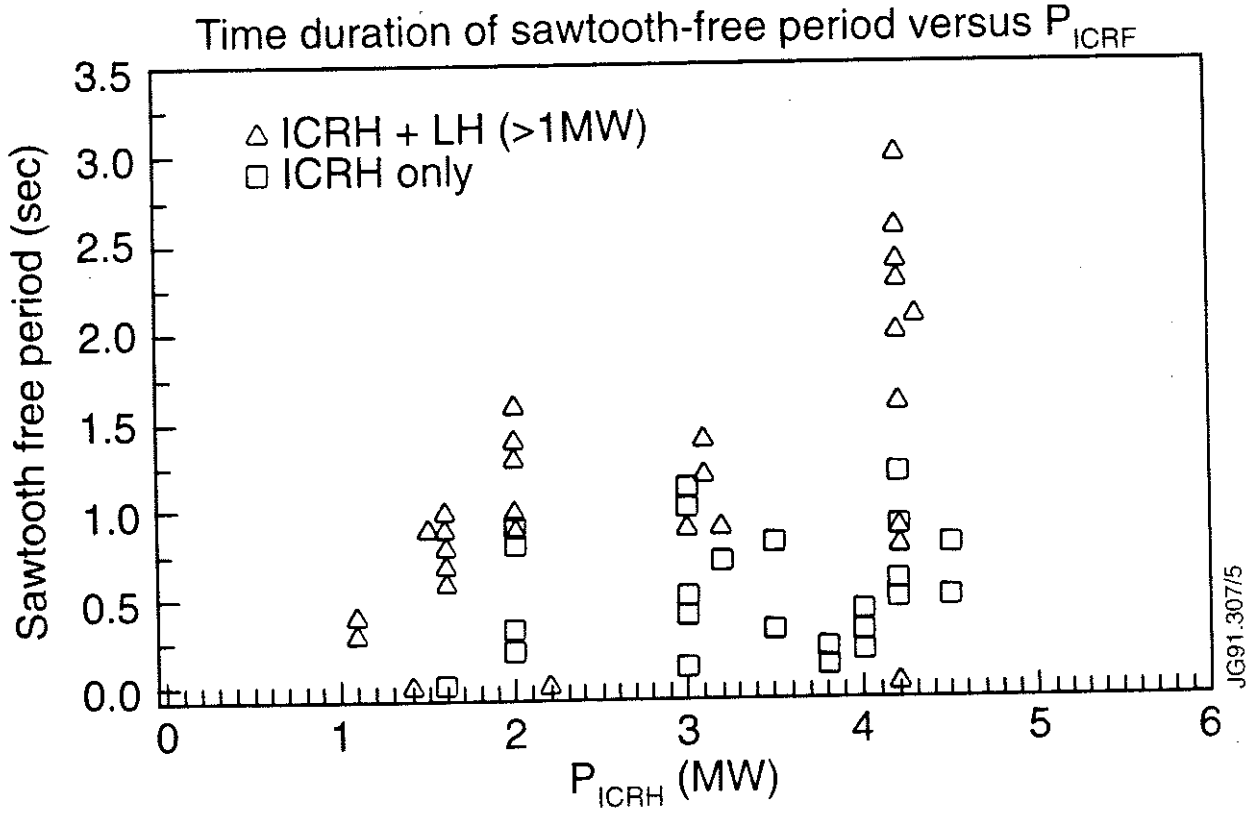

fig.22 - Sawtooth period vs. applied ICRH and LH power.

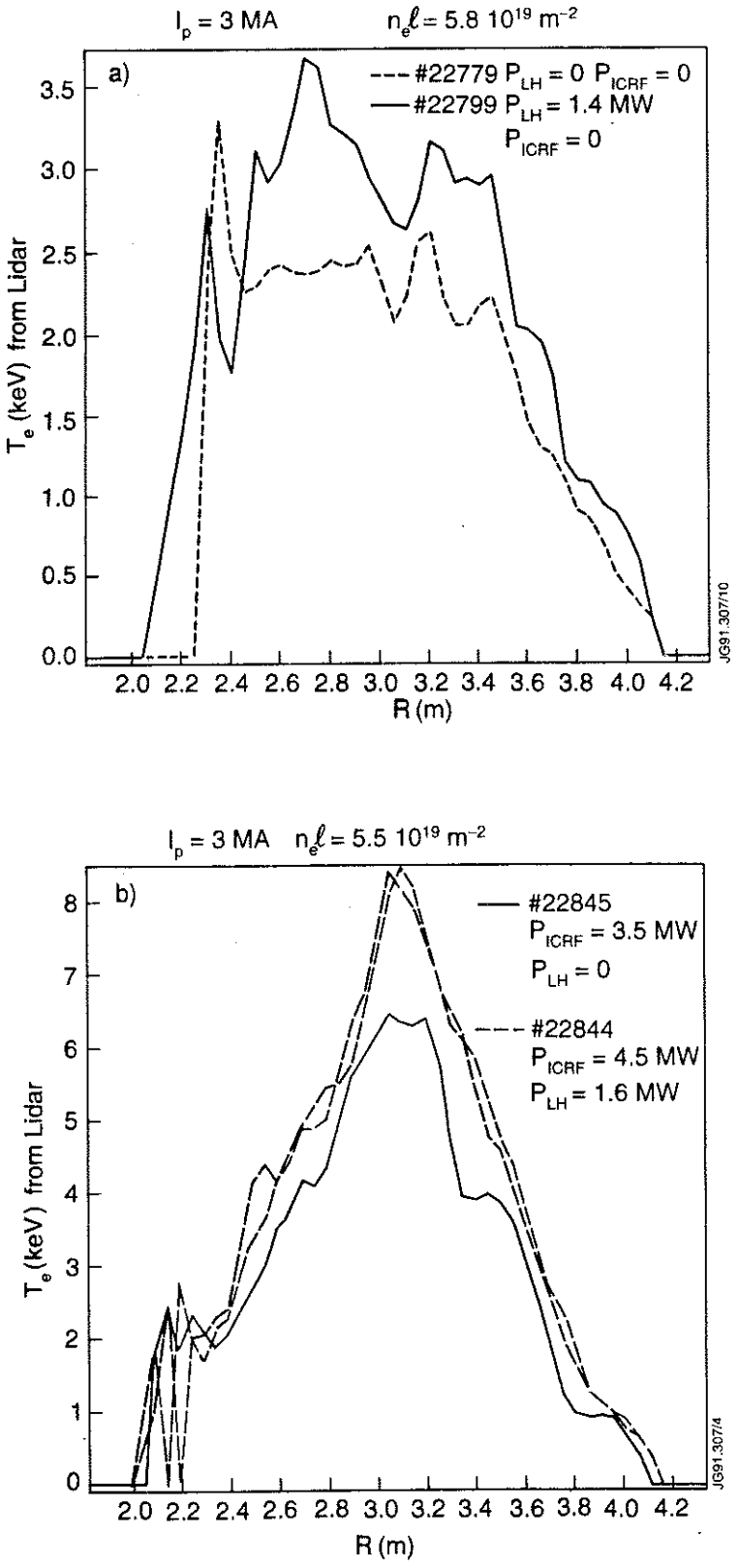

fig.23 - Electron temperature profile vs. plasma major radius, as measured by the LIDAR diagnostic, indicating electron heating during LH in (a) Ohmic discharges and (b) in combination with ICRH. The peaking observed in (b) is associated with higher current drive efficiency.

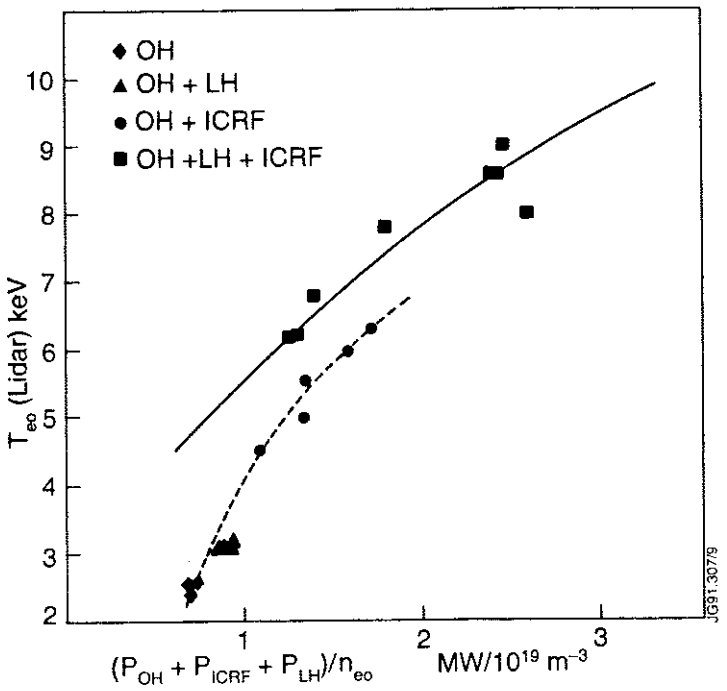

fig.24 - Behaviour of the central electron temperature as measured by the LIDAR system vs. the power per particle parameter.

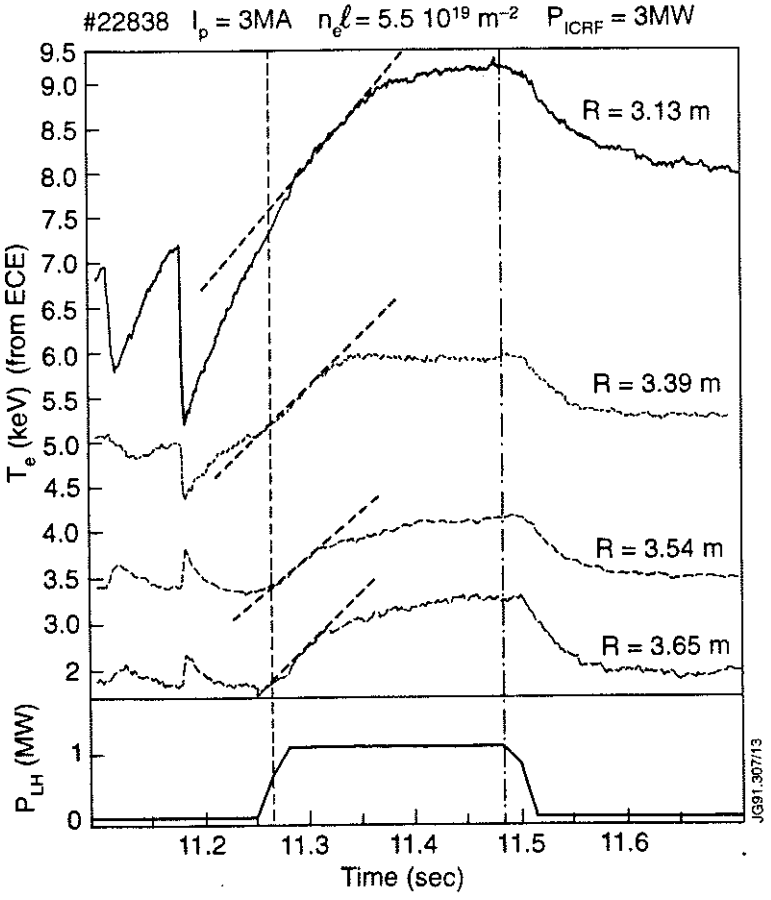

fig.25 - Time evolution of the local electron temperature, as measured by the ECE Fabry-Perot Interferometer, during LH modulation.

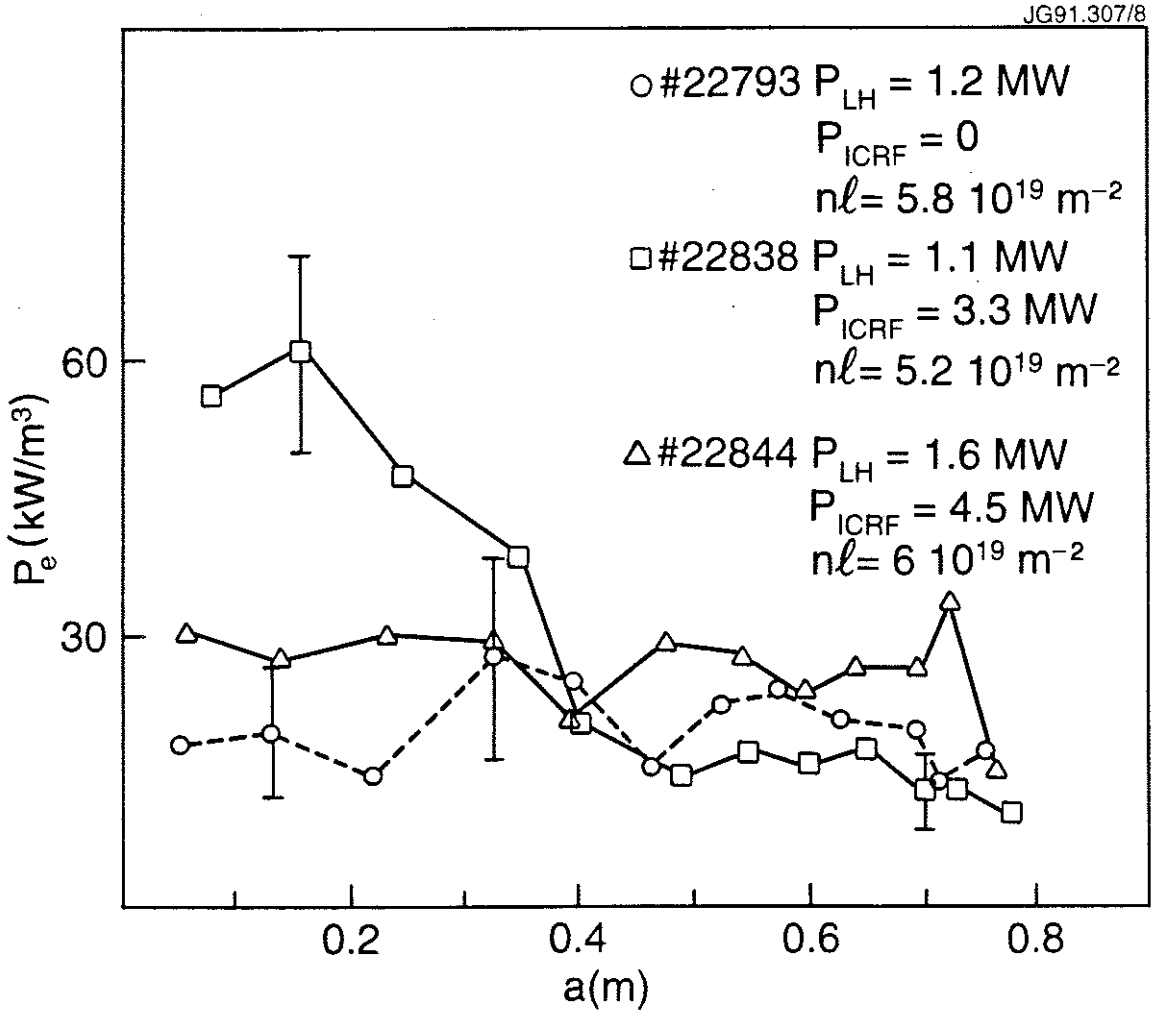

fig.26 - Electron heating power deposition profile vs. plasma equatorial minor radius during LHCD in Ohmic and ICRH discharges for different power and plasma density values.